

## Review paper

## Super-resolution optical imaging: A comparison

Gergely Huszka \*, Martin A.M. Gijs

Laboratory of Microsystems, École Polytechnique Fédérale de Lausanne, 1015 Lausanne, Switzerland

## ARTICLE INFO

## Keywords:

Optical super-resolution microscopy  
Far-field imaging  
Near-field imaging  
Micro-objects  
Microspheres  
Photonic nanojet

## ABSTRACT

Overcoming the classical diffraction limit in optical microscopy is known to be achievable by a variety of far-field and near-field microscopy techniques. More recently, so-called micro-object-based optical super-resolution microscopy techniques have emerged. In this review, we provide an overview of the state-of-the-art of optical super-resolution imaging techniques. In the first section, far-field techniques are discussed, which can be considered as advanced classical optical microscopy methods that mostly operate with fluorescent samples. In the second section, near-field techniques are presented that achieve super-resolution by maintaining a close distance between a nanometric detection unit and the sample, such that evanescent waves can be captured and processed. Near-field methods typically involve some scanning procedure to be able to map a reasonably large area of the sample. In the third section, dielectric micro-object-based techniques are discussed. These provide a more recent, practical and affordable alternative to the other super-resolution microscopies. Finally, we provide a comparison of the presented techniques in terms of performance and cost, pointing out the application-specific strength of each imaging method.

© 2018 The Authors. Published by Elsevier B.V. This is an open access article under the CC BY-NC-ND license (<http://creativecommons.org/licenses/by-nc-nd/4.0/>).

## Contents

1.	Introduction . . . . .	8
2.	Far-field super-resolution techniques . . . . .	8
2.1.	Confocal fluorescence microscopy . . . . .	8
2.2.	Point spread function engineering-based microscopy . . . . .	8
2.3.	Moiré effect-based microscopy . . . . .	10
2.4.	Spatially modulated illumination microscopy . . . . .	10
2.5.	Single molecule localization microscopy . . . . .	11
3.	Near-field super-resolution techniques . . . . .	12
3.1.	Photon tunneling microscopy . . . . .	12
3.1.1.	Near-field scanning optical microscopy . . . . .	13
3.1.2.	Tip-enhanced near-field optical microscopy . . . . .	14
3.2.	Photon scanning tunneling microscope . . . . .	14
3.3.	Near-field optical random mapping nanoscopy . . . . .	14
4.	Micro-object-based super-resolution imaging . . . . .	15
4.1.	Physics of the photonic nanojet . . . . .	15
4.2.	Experimental evidences for the photonic nanojet . . . . .	16
4.3.	Towards larger dielectric micro-objects for increased field-of-view imaging . . . . .	18
4.4.	Dielectric microsphere-based scanning systems . . . . .	21
5.	Discussion . . . . .	24
	Conflict of Interest Statement . . . . .	25
	Acronyms . . . . .	25
	Symbols . . . . .	25
	Acknowledgements . . . . .	25
	References . . . . .	25

\* Corresponding author.  
E-mail address: [gergely.huszka@epfl.ch](mailto:gergely.huszka@epfl.ch) (G. Huszka).

## 1. Introduction

It was Ernst Karl Abbe, who laid down the basics of modern microscopy together with Otto Schott and Carl Zeiss at the end of the 19th century. Abbe's most significant contribution was the law named after him, which describes the relation between the diffraction limit (*i.e.* lowest detectable feature laterally ( $d_{x,y}$ ) and axially ( $d_z$ ) with respect to the light propagation direction, respectively in Eqs. 1a and 1b), the wavelength of the light ( $\lambda$ ) and the numerical aperture ( $NA$ ):

$$d_{x,y} = \frac{\lambda}{2 \times NA} \quad (1a)$$

$$d_z = \frac{2 \times \lambda}{NA^2}. \quad (1b)$$

This simple equation immediately showed the limit of optical microscopes in terms of lateral resolution and also the two possible development directions to overcome this restriction. To reach smaller  $d$ , either the wavelength must be smaller or the  $NA$  bigger. Various techniques achieving the latter or applying other methods to overcome this limitation will be discussed in the following sections. On the other hand, techniques involving wavelengths outside the visible light region will not be discussed here since the scope of this review focuses on optical methods.

Breaking the diffraction limit by optical super-resolution imaging was demonstrated already in the 1980s and '90s', including both near-field and far-field optical imaging techniques. The latter became extremely popular in the last decade as development of various fluorescent dyes facilitated optical super-resolution imaging of biological samples. These developments were reviewed in multiple papers [1–4]. Similarly, near-field super-resolution imaging was also already reviewed [5,6], but it is important to point out that these specialized papers did not provide a general overview about all super-resolution imaging principle. A relatively new approach to optical super-resolution imaging, called micro-object-based imaging has emerged during the last decade. Although both the use of dielectric microobjects in microfluidic applications [7] and their associated phenomenon, the photonic nanojet (PNJ) [8] was already reviewed, no general comparison between the three approaches was presented yet. In our paper, we focus on showing in parallel the three branches of far-field, near-field and micro-object-based optical super-resolution microscopy. We (i) explain the imaging principles of all three approaches, (ii) present in more detail the novel imaging applications offered by the use of dielectric micro-objects and (iii) provide a comparison of the presented techniques in terms of lateral resolution, field-of-view, imaging time and cost-effectiveness.

## 2. Far-field super-resolution techniques

Initially it seemed impossible to overcome the diffraction limit by detecting the propagating waves emerging from a sample placed under a microscope (*i.e.* with far-field microscopy). The motivation for wanting super-resolution imaging arrived from biology and, the breakthrough came, when fluorescence-based super-resolution imaging techniques started to be developed in the beginning of the 1990s.

### 2.1. Confocal fluorescence microscopy

One of the first methods to achieve super-resolution was the 4Pi microscopy that was patented in 1990 [9] and its description was published in 1992 [10]. The significant improvement compared to confocal fluorescence microscopy (CFM) was to introduce two opposing microscope objective lenses for illumination and detection. A confocal system has an illumination and a detection intensity distribution which are described by the illumination-and detection-point spread

function (PSF), respectively. Multiplying these two gives the confocal PSF, which determines the lateral and axial resolution of the system. Introducing a second microscope objective to such a system can increase the aperture of the system in two ways. Either the objectives generate coherent illumination wavefronts that constructively meet in the common focus or the collected fluorescent lights interfere constructively in the common point detector. This criteria enables three operation mode for the 4Pi microscope: type A) illumination interference [11]; type B) detection interference [12]; type C) illumination and detection interference [10].

The first presented imaging setup of the 4Pi microscopy consisted of a light amplification by stimulated emission of radiation (*laser*) light source that was split towards the two objectives and the detected fluorescent signals were directed into the same photomultiplier. The sample was placed on a motorized stage that allowed 5 nm steps over 20  $\mu$ m distance for scanning. With this instrument, a fourfold increment in the axial resolution was demonstrated, compared to the classical CFM setup, as the full width at half-maximum (FWHM) of the central peak originating from a point-like source was measured to be 110 nm. It was also shown that the instrument can operate in two-photon excitation mode, which can further improve the achievable resolution [11]. A general advantage of the 4Pi microscope is that only half the light intensity is needed to expose the sample, therefore it gives better protection against out-of-focus bleaching. Furthermore, it can reach the same intensity and signal-to-noise ratio (SNR) as CFM, but with smaller probe volume.

### 2.2. Point spread function engineering-based microscopy

The introduction of 4Pi microscopy showed that Abbe's resolution limit can be overcome in the axial direction, when imaging fluorescent samples. Achieving the same improvement in the lateral direction was showed only a few years later [13]. The technique was called two-photon excitation fluorescent light microscopy. The concept of this imaging setup was to place two point-like excitation sources laterally, to generate an overlap of their PSF in the focal plane of the imaging objective. It was shown that the PSF can be significantly narrower depending of the offset of the two light sources. A limitation of the offset positions is the appearing side lobe in the PSF. This would decrease the image quality, but can be suppressed with a point-like (*i.e.* confocal) detection. Another issue is that as the offset increases, the probability of the two-photon excitation decreases, as the overlap of their PSF becomes smaller and smaller. The offset between the excitation points can be achieved in two ways. Either two light sources with different wavelength are needed or a femtosecond *laser* must be used. If the latter is employed, each pulse has to be split into two and these separate pulses have to be laterally displaced and temporally delayed in relation to each other [13]. It was shown that with offsetting, the PSF can be reduced up to 59%, which corresponds to 75 nm lateral resolution considering visible light and conventional optics.

As an improvement of the two-photon excitation technique, stimulated-emission-depletion (STED) fluorescence microscopy was developed [14]. It is known that the PSF determines the resolution of a scanning fluorescent microscope and that reducing its spatial extent is the key to improvement. A way of reduction, as presented in this imaging system, is to inhibit the fluorescence in the outer regions of the PSF. In order to understand how that is possible, the energy levels of a typical fluorophore have to be considered as shown in Fig. 1. The  $L_0 \rightarrow L_1$  transition is induced by the point source (*i.e.* a *laser* focused onto a pinhole). The  $L_1 \rightarrow L_2$  and  $L_3 \rightarrow L_0$  transitions are due to vibrational relaxation, meanwhile the  $L_2 \rightarrow L_3$  is the spontaneous emission that is three orders of magnitude faster, than the first two. This time difference allows the interaction that is the key element of the STED technique. If a second *laser* is introduced into the system, it is possible to artificially induce the  $L_2 \rightarrow L_3$  transition, therefore depleting the excited state before fluorescence takes place.

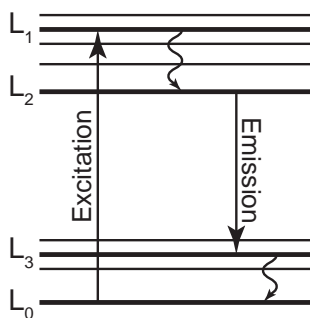


Fig. 1. The possible energy levels of a typical fluorophore.

In practice this is achieved by placing a secondary (*STED*-)laser next to the primary excitation laser. The secondary beam is split into two and focused to the focal plane with a  $\pm 3 < \nu < 7$  optical unit offset. The optical unit  $\nu = 2\pi r NA / \lambda_{exc}$  where  $r$  is the distance from the focal point,  $NA$  is the numerical aperture of the objective lens and  $\lambda_{exc}$  is the excitation wavelength (i.e. the wavelength of the primary laser). Before reaching the focal plane, the light travels through a phase plate that generates a donut-shaped energy distribution and thus realizing the earlier mentioned inhibition of the outer regions of the excitation PSF, created by the primary laser. The depletion and the correlation resolution increment caused by these beams depends on their intensity values. Assuming  $\lambda = 600$  nm wavelength and  $1300$  MW/cm<sup>2</sup> intensity for the *STED*-laser, the PSF can be narrowed to reach a resolution increment of 3.4 and 4.5 times compared to CFM and conventional fluorescent microscope, respectively. Calculating for a dye that can be excited at  $\lambda = 490$  nm and an emission at  $\lambda = 600$  nm, this means 50 nm lateral resolution using  $NA = 1.4$  objective and setting the *STED*-laser to  $\Delta\nu = 3.9$  offset. Altering the dye emission wavelength to the low-end of the visible light spectrum (i.e. to 400 nm) would result in 35 nm resolution, which is deeply below the classical resolution limit. The price of such a big resolution enhancement ( $\sim 3$  times) is the signal strength which is only  $\sim 25\%$  of a conventional microscope's one. Furthermore, the beam intensities are typically in the  $10^8$  to  $10^{10}$  W/cm<sup>2</sup> range, which is considerably high [16]. Despite of this, these results place this imaging method to one of the top ranking in far-field light microscopy techniques, since it has such a high lateral resolution, which is even comparable with near-field techniques. The development of this microscopy was awarded with the Nobel-price in chemistry in 2014 [17].

As an improvement in further exploiting the resolution decreasing effect of the stimulated depletion, ground-state-depletion (GSD) fluorescence microscopy was reported in 1995 [15]. This concept showed how it is possible to achieve  $\sim 10$ – $20$  nm lateral resolution with low-power continuous-wave illumination. Because of the specific illumination type, the triplet state plays a significant role in the possible energy states of the fluorophore. As Fig. 2a shows, above  $10$  MW/cm<sup>2</sup> intensity, the ground state is depleted, as all the molecules are in singlet or triplet state. Calculating the PSF for different intensities show how much resolution gain can be achieved (Fig. 2b). In the case of  $1$  MW/cm<sup>2</sup> intensity, this enhancement is six-fold, compared to a classical scanning fluorescent microscope, but having a fluorophore with faster inter-system crossing time can increase this value to eleven-fold. The latter would mean 15 nm lateral resolution using  $NA = 1.4$  objective and a fluorescent dye with  $\lambda_{exc} = 400$  nm. To reach this intensity at the focal plane with the objective used for the previous calculation, only 1 mW illumination power is needed, which is not extraordinary from a practical point-of-view. Technically there are no other factors that would hinder experimentation, as recording time can be comparable with a standard scanning CFM and the chemical environment can be adjusted to hinder photo-bleaching.

Despite of the clear concept, the realization of this microscopy technique was not pursued until 2007 [16]. The breakthrough happened by

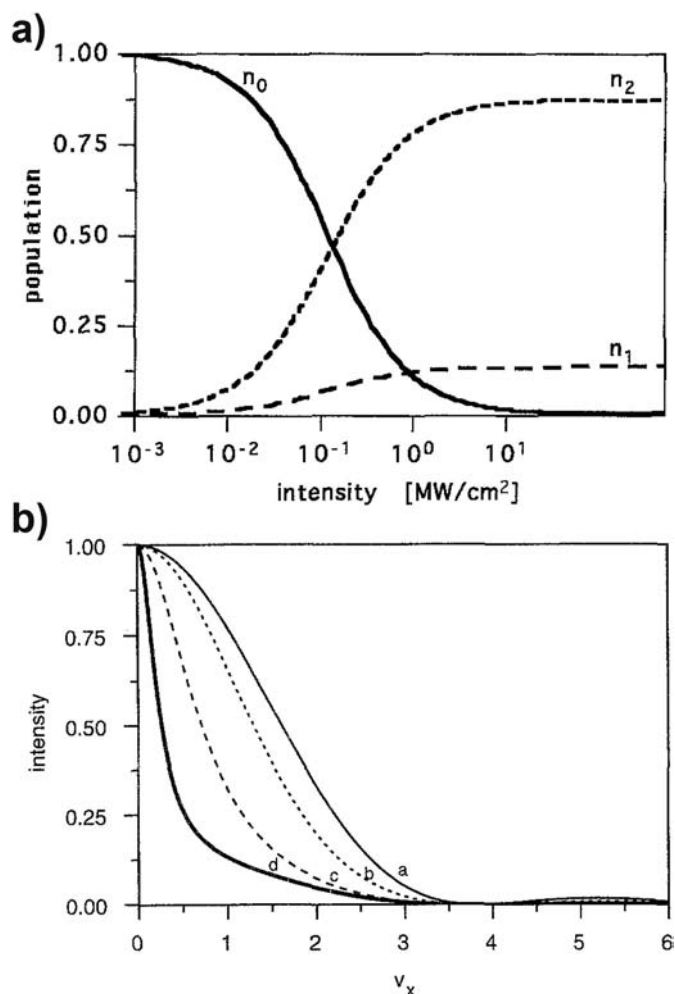


Fig. 2. Population probability and effective point spread function in GSD fluorescence microscopy. a) The population probability of the ground state ( $n_0$ ), the first singlet state ( $n_1$ ) and the triplet state ( $n_2$ ) as a function of the excitation intensity. b) The effective PSF along the focal plane in the case of 0.01 (b), 0.1 (c) and 1 (d) MW/cm<sup>2</sup> intensity depletion beam (GSD technique), compared to a classical scanning fluorescent microscope (a). Reprinted by permission from Springer Nature: [15].

discovering conditions at which  $\mu$ s- and ms-long optical shelving is practical, with special attention to the chosen combinations of dyes and media. The other critical factor was the light intensity used for depletion. The resolution of GSD fluorescence microscopy is given by the following equation,

$$d \approx \frac{\lambda}{2 \times NA \sqrt{1 + \frac{I_D^{MAX}}{I_S}}}, \quad (2)$$

where  $I_D^{MAX}$  is the depletion beam intensity and  $I_S$  is the saturation intensity at which half of the fluorescence is depleted. Eq. 2 implies that the depletion beam intensity should be increased as high as possible to reach the lowest resolution, however, this would cause an imminent photo-bleaching. Therefore practically depletion intensity values are in the kW/cm<sup>2</sup> range. The low intensity normally means longer recording time, but this was compensated by a special image recording technique and processing algorithm. With such an illumination condition 50 nm – 90 nm lateral resolution was reached, depending on the shape of the depletion beam in the focal plane. Although these values were higher than the theoretical predictions presented in [15], further improvements in

the imaging system showed that lateral resolution down to  $\approx 7.6$  nm can be reached with this microscopy technique [19].

### 2.3. Moiré effect-based microscopy

Structured illumination microscopy (SIM) was patented in 1995 [20], but its full description was presented only in 2000 [18]. The motivation behind this development was to be able to improve the lateral resolution, since existing CFM-based techniques suffered from a limitation set by the used pinhole sizes. To achieve smaller resolution, a smaller pinhole is needed, but that discards much of the in-focus emission light together with the unwanted out-of-focus light. On the other hand, biological samples often produce a very weak signal, therefore, a larger pinhole is needed for their detection. However, by increasing the size of the pinhole, the resolution enhancement becomes minimal and eventually negligible.

The concept behind SIM can be explained by a simile with Moiré fringes. If two patterns with fine details are superposed multiplicatively, a third, coarser pattern will appear (Fig. 3a). If only one of the fine patterns and the superposed pattern is known, the other fine pattern can be calculated. Translating this idea to microscopy shows how imaging is performed. One of the fine patterns is the spatial distribution of the fluorescent dye, that needs to be imaged. The other fine pattern is the structured excitation light intensity. The superposed pattern is given by these two and can be observed with the microscope setup. Considering a conventional microscope with diffraction  $d_0$ , its resolution capabilities can be represented as a circle with radius  $1/d_0$  in Fourier space (Fig. 3b). Applying structured illumination to this system does not increase the radius, but makes it possible to involve information from outside it. As an example, a sinusoidal stripe pattern is considered (Fig. 3c). Such pattern has three non-zero points in Fourier space, from which two is in offset from the origin. Their position is determined by the direction and line spacing of the illumination pattern, but the distance from the origin cannot exceed the original radius. Upon imaging, Moiré fringes will appear that contain information – that would be impossible to get with a classical microscope – from these offset regions (Fig. 3d). By repeating this operation with differently oriented patterns, it is possible to double the size of the observable region (Fig. 3e).

The instrumentation needed to construct SIM does not differ significantly from a confocal microscope. The main difference between the two is a diffraction grating that is used to generate a high-contrast stripe pattern with feature size close to the resolution limit of the attached microscope objective. Furthermore, this grating has to be able to rotate for enabling the full imaging potential of the instrument. Experimental results showed that lateral resolution can be significantly improved with this technique. While only 290 nm FWHM features were detected by a conventional microscope, SIM could improve that more than two-fold, down to 115 nm. Exposure times of 1–10 s were reported with an additional 30 s processing time. This included parameter fitting and did not use any *a priori* information. If the latter is used for the computation,

the process could be speeded up to near real time, since the method is linear and deterministic.

An improved version of SIM, achieving 50 nm lateral resolution was reported in 2005 [21]. This advanced wide-field imaging technique was called saturated structured illumination microscopy (SSIM). The non-linearity arising from the saturation of the exciting light allowed to further decrease the resolution limit. To achieve this, long exposure times were needed, which made *in vivo* imaging difficult. For the same reason, photostable and brightly labelled samples are obligatory in this method.

### 2.4. Spatially modulated illumination microscopy

The first prototype of spatially modulated illumination (SMI) microscope was built in C. Cremer's laboratory in Heidelberg in 1997 [22,23]. It utilized interferometric illumination combined with optical sectioning to achieve high precision localization and resolution increment along the optical axis. The setup consisted of a coherent light source that was separated and lead into two objectives which were placed on the opposite side of the sample. The light was linearly polarized, collimated and interfered under an angle  $\nu$ . The convolution of the PSF of the resulted fringe pattern and the PSF of the object's fluorochrome distribution resulted in the image of the sample objects. For three-dimensional (3D) localization, scanning of the image planes was needed. Because of the special illumination pattern, the axial resolution was decreased to the half-distance ( $d/2$ ) between the wave fronts. Such an improvement enabled localization with nanometer precision.

While the first prototype consisted of only one coherent light source, later developments applied a second one to allow the localization of different spectral signatures independently [24]. The key optical components were very similar in both cases. The light was divided evenly by a beam splitter and focused to the back focal plane of both objectives by two lenses. To control the length of one of the light paths, a piezoelectric motor was placed between the beam splitter and the focusing lens. Another piezoelectric element was controlling the stage movement along the optical axis, which was needed for 3D scanning. All of the components were assembled on a thermally stabilized breadboard to conserve the stability of the illumination pattern during the image acquisition. For that, typical reported times were between 2 and 4 s per image plane. Therefore a sample volume of  $\sim 50 \mu\text{m} \times 50 \mu\text{m} \times \sim 10 \mu\text{m}$  could be imaged in  $\sim 25$  min. Although imaging is not immediate, its accuracy is remarkable as both axial and lateral resolution was in the nanometer range [22–25].

A significant improvement was reported in 2008, when a full upright positioned imaging system was built on the bases of the SMI microscope prototype. The setup was upgraded to have three different wavelength coherent light sources and a white light emitting diode (LED) to reduce photo-bleaching during the initial search for the focal plane. Further additions like water-immersion objectives instead of oil-immersion ones, incubator chambers for cell cultures, air-flow and temperature control enabled near-real time observation of live cells. Finally, data acquisition speed was increased to reduce the imaging time to  $\sim 2$  s. It was also

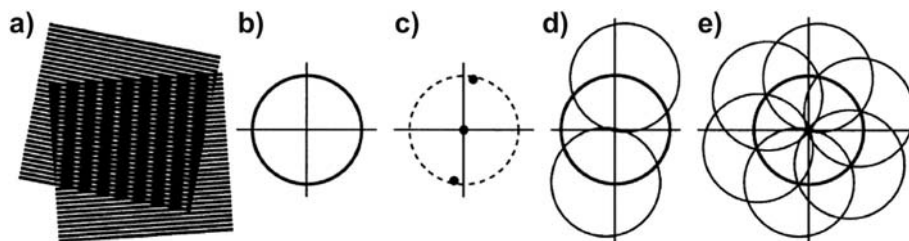


**Fig. 3.** The concept behind SIM. a) Two fine patterns are superposed, generating Moiré fringes. b) The observable region of a conventional microscope in Fourier space. c) A sinusoidally striped illumination pattern that has three Fourier components, from which two is on the side and their position is limited by the same circle as in b). d) Upon illumination, Moiré fringes will appear that represent information that changed position in the Fourier space. Therefore the observable region will be expanded with additional information, originating from the two offset regions. e) Repeating this method in sequence leads to recovering information from an area up to twice the size of the original observable region. This corresponds to twice the normal resolution. Reprinted by permission from John Wiley and Sons: [18].



shown that this instrument can be operated both in “SML” and “2D localization” mode. (Localization methods are detailed in the following paragraph.) The former offers excellent axial resolution (44 nm diameter microspheres ( $\mu\text{S-s}$ ) were imaged), meanwhile the latter has superior resolution in one image plane ( $\sim 15$  nm localization accuracy was demonstrated).

### 2.5. Single molecule localization microscopy

Single molecule localization microscopy (SMLM) hallmarks a branch of computational-based microscopy techniques that achieve super-resolution by precision distance and position measurements of individual emitters. The algorithmic basis behind these processes was established in 1997 [26,27]. Originally, the algorithm was designed for high-precision distance measurement and for volume-conserving segmentation of fluorescent samples. Its accuracy was only given as an upper estimation of less than 60 nm, due to the unoptimized routine and experimental parameters. These results were obtained on a simulated data set and the evaluation took 3–10 min. Note, that at that time a 200 MHz clock frequency processor with 96 MB memory was used, which has multiple times less computational capacity than an entry-level consumer smartphone in 2018. Even under these conditions, the limitations of the method were already shown, namely, that there must be a minimal distance between the individual points, otherwise the algorithm can merge multiple objects. This indicates that dense populations must be separated with a method that generates different spectral signature for the individual targets or for a sub-population of them. The concept was validated experimentally by measuring clusters of monodisperse quartz glass spheres [26] and pentacene molecules embedded in a *p*-terphenyl host crystal [28]. The former experiment achieved 15 nm lateral resolution in-plane and 55 nm out-of-plane, meanwhile the latter demonstrated 40 nm laterally and 100 nm axially. This technique was later referenced as spectral precision distance/spectral position determination microscopy (SPDM).

A new approach in localization microscopy was presented in 2005, when it was shown that super-resolution can be achieved with intermittent fluorescence of quantum dots and independent component analysis [29]. This type of analysis can separate the individual sources from the convoluted signals provided by the detectors (*i.e.* the pixels in the charge-coupled device (CCD)), if the following four criteria are met: (i) the individual fluctuations of the source must be statistically independent – quantum dots meet this condition; (ii) the probability distribution must be non-Gaussian – sampling in short time transforms the distribution into bimodal (*i.e.* on-off like); (iii) the convoluted detection

signals, originating from the ensemble of sources, are linear combinations from the individual source signals and the latter need to be sufficiently apart, so that they are distinguishable at a given moment in time; (iv) the number of detectors is equal or greater than the number of sources – this would set a limit to the number of separable sources but can be increased with oversampling. The concept was experimentally proven as a set of 500 images of  $256 \times 256$  pixels size were taken and processed, showing finally the image of quantum dots with  $\sim 20$  nm lateral resolution in 2D.

A further reflection of this idea is the photoactivated localization microscopy/fluorescence photoactivation localization microscopy (PALM/FPALM) [30,31]. The two techniques were published only with a few months of difference by two different research groups, but the principle of them is the same and shown in Fig. 4. Two lasers are utilized for illuminating the sample, one for readout and one for activation. The latter one turns “on” with a brief pulse some of the fluorescently labelled targets in the sample, which are imaged and localized by the post-processing algorithm. Due to the imaging with the read-out laser, these targets get photo-bleached with time and irreversibly turn into dark, meanwhile new targets are activated by a new pulse. This cycle is repeated until enough information is gathered to construct the final super-resolution image. The process can take up to several hours depending on the desired quality of the final result. In optimal conditions  $\sim 10$  nm lateral resolution was shown in fixed thin slices [31]. It was also demonstrated that this technique can be used *in vivo*, in this case  $\sim 40$  nm lateral resolution was achieved [32]. Although the resolution capabilities of this method are superb, the PALM/FPALM suffers from three major inconveniences: (i) it is sensitive to diffuse background, therefore its suppression is needed (*e.g.* by using total internal reflection fluorescence microscopy); (ii) usually thin samples are needed; (iii) acquisition times can be huge (up to 12 h).

To overcome these issues, an improved method, called PALM with independently running acquisition (PALMIRA) was developed in 2007 [33]. The exposure time of a fast CCD camera was matched with the average on-time of a novel, reversibly switchable fluorescent protein. Since this protein could be switched on and excited at the same wavelength, one laser light source was enough in the setup. Furthermore, because no synchronization was needed between the excitation and the readout, the data collection time could be significantly improved. This was possible, because during imaging a dynamic equilibrium was formed by these molecules, in which most of them were in the dark state and only a small fraction was activated in random times. This activation crosstalk, which was practically the  $\sim 0.2\%$  probability of on-state proteins at a time was the key component that enabled all of the

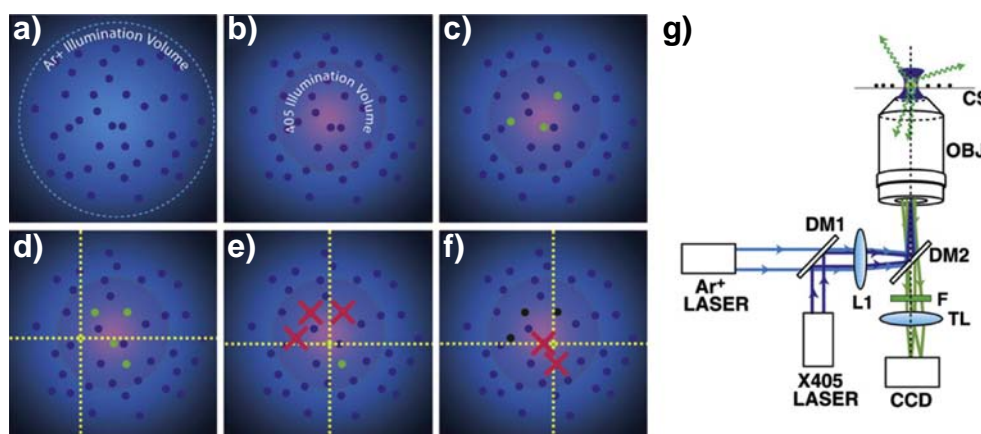


**Fig. 4.** Principle and schematic of PALM/FPALM. Spatial illumination profile of a) the readout laser ( $\text{Ar}^+$  ion laser) and b) the activation laser (405 nm diode laser). Some of the fluorescently labelled samples are activated (green dots) within the illumination region c) and localized d). e) As targets photo-bleach due to overexposure (red crosses), they become irreversibly dark, meanwhile new targets get activated f). The process is repeated until sufficient amount of signal is detected for super-resolution imaging. g) Schematic of the microscope setup. Sample (CS) is illuminated with two lasers through a focusing lens (L1) and two dichroic mirrors (DM1 and DM2). Emitted fluorescence from the sample arrives to the camera (CCD) through a filter (F) and focusing lens (TL). Reprinted by permission from Elsevier: [30].

aforementioned improvements. Due to the asynchronous 500 Hz camera frame rate, background suppression was not needed any more. Imaging experiments showed  $\sim 50$  nm lateral resolution with total acquisition time of  $\sim 2.5$  min including all image processing. However, these outstanding results were achieved at a cost of narrowing the possible sample classes to reversibly switchable fluorophores.

Parallel to PALM/FPALM, a very similar localization technique, stochastic optical reconstruction microscopy *STORM* was introduced in 2006 [34]. Its governing principle was based on switching fluorescent molecules on and off with two, different colour *laser*. The cycling process started with turning all molecules into the dark state with a pulse generated by the red *laser* ( $\lambda = 633$  nm). This pulse did not permanently photo-bleach the molecules, but converted them into a photo-reversible non-fluorescent state [35]. Then a short pulse from the green *laser* ( $\lambda = 532$  nm) arrived that turned on (i.e. converted back to fluorescent state) a subset of the fluorophores in a way that the population density was low enough for accurate localization. After this pulse the red *laser* served as excitation until the probes were turned off again. This cycle was repeated until sufficient amount of information was collected to construct the final image of the sample. It was also shown that the deoxyribonucleic acid (DNA)-bound Cy5 switch can be turned on and off hundreds of times before permanent photo-bleaching occurs. For the same sample, 20 nm lateral resolution was demonstrated.

Other variations for the *STORM* were reported two years later. Three different laboratories developed almost the same concept alongside. The new techniques were named direct *STORM* (*DSTORM*) [36], ground state depletion microscopy followed by individual molecule return (*GSDIM*) [37] and reversible photo-bleaching microscopy *RPM* [38], respectively. Instead of activation, these methods forced the fluorophores into their triplet state (or another metastable dark state) and recorded them as they slowly returned. Since the speed of this process could be regulated to be low enough for the earlier detailed localization processes, super-resolution imaging with lateral resolution of 20–30 nm was possible. Since multiple research groups were exploring this method, already at the time of first publications, a wide range of experimental imaging was demonstrated, including that of microtubules and actin filaments labelled with various dyes, showing the great imaging potential of this microscopy system. As for realization, imaging systems built on different approaches were used, since this technique could be implemented in a single inverted microscope with special immersion (such as polyvinyl alcohol, mercaptoethanol or glucose oxidase) [37] or in a total internal reflection microscope with low refractive index (*RI*) media [38]. However, a common drawback of all *STORM*-based techniques is that they need to collect a huge amount of data to perform the image processing, therefore generating a single picture can take minutes.

It was also demonstrated that super-resolution can be reached not only by advanced instrumentation, but by smart image processing too. A fine example of this is the super-resolution optical fluctuation imaging (*SOFI*), first presented in 2009 [39]. This method relies on the independent stochastic fluctuations of the emitters and needs three criteria to be fulfilled: (i) the fluorescent label has to be able to exhibit at least two optically distinguishable states; (ii) the switch between these states must be stochastic; (iii) the image should be acquired with pixels smaller than the diffraction limit. However, it was shown in a later publication that the third criteria can be overcome with an adjusted algorithm [40]. The principle of *SOFI* is based on the spatio-temporal evaluation of the optical signal by taking a series of pictures of the sample and subsequently calculating the temporal  $n^{\text{th}}$  order cumulant for each pixel. Plotting these yields a final picture with  $\sqrt{n}$  resolution increment. As experimental demonstration, 55 nm lateral resolution was achieved by calculating the 25th order while imaging quantum dots. Although this value is higher than other localization methods (shown earlier in this section), it is very important to see that no special electronics

or acquisition schemes were needed. However, the first two criteria still impose a restriction that has to be kept in mind when applying this microscopy technique.

After a decade, the development of different localization microscopy techniques still did not slow down. Label-free version of *SPDM* was shown in 2011 [41]. It was demonstrated that cellular structures can be imaged with 20 nm resolution only by detecting the fluorescent signals emerging naturally from within the cells. In the same year, a technique called binding-activated localization microscopy (*BALM*) was developed, utilizing the strong fluorescent signal, generated, when certain dyes bind to DNA [42]. Mapping these individual events allowed super-resolution imaging of bacteria with  $\sim 14$  nm lateral resolution. Although these findings were widening the potential application fields of localization microscopies, they did not reach a significant breakthrough in terms of resolution, since sub-20 features were already imaged with the earliest localization techniques [26]. However, cryogenic optical localization in 3D (*COLD*) was shown recently, which enabled mapping multiple fluorescent sites of a protein with Angstrom resolution [43]. For this microscopy technique, the sample had to be cooled down to 4.3 K. At this temperature, stochastic photo-blinking becomes way longer, its duration reaches above the second range. Atto647N type dye was used for demonstration with which binding sites could be imaged. Since the range of the measurements were in the Angstrom region, dimensions of the fluorescent label and its linker became a limiting factor of the accuracy. Nevertheless, this microscopy technique reached one of the highest resolution in optical imaging, although the needed temperature environment still remains a limiting factor.

During the last decades of far-field optical super-resolution development, many concepts evolved into a commercial product. Based on the comparison provided by [3], the advantage of these techniques in terms of both lateral and axial resolution over the *CFM* is very clear. However this comparison ignores several important influencing parameters (e.g. field-of-view, cost of the imaging system), which are discussed in Section 5.

### 3. Near-field super-resolution techniques

It is also possible to reach super-resolution without fluorescent labelling. For that, the information coded in the evanescent waves must be resolved (i.e. near-field imaging is needed). Evanescent waves are non-propagating electromagnetic waves, whose energy is spatially concentrated in the vicinity of the source, therefore they decay exponentially with distance from their originating surface [44]. Due this behaviour, they only can be collected by placing in the vicinity of the sample a probe that can act as a transducer. However, such a tiny probe would typically limit the field-of-view (*FoV*). A logical solution is to implement a scanning technique, such as the well-established scanning tunneling microscopy (*STM*) [45] or atomic force microscopy (*AFM*) [46], and therefore combine this instrumentation with optical attachments to create a near-field optical imaging system.

#### 3.1. Photon tunneling microscopy

Photon tunneling microscopy (*PTM*) was reported by J. M. Guerra in 1990 [47]. This instrument utilizes the so-called photon tunneling effect, which determines how a photon behaves, when it arrives from a medium with higher *RI* [ $n_1$ ] to one with lower *RI* [ $n_2$ ]. If the photon reaches the boundary at a critical angle [ $\sin^{-1}(n_2/n_1)$ ] or larger, it will tunnel into the new medium and simultaneously generate an electric field there. But because no energy is transferred, total internal reflection will happen, therefore the generated field in the new medium will be evanescent. As such, it is exponentially decaying with the penetration depth, normal to the boundary. However, if a third medium with *RI* [ $n_3 > n_2$ ] is present, coupling will appear causing a complex interaction. This can cause an inverse and exponential change in the energy transfer,

enabling to detect the topography of medium 3 (i.e. the vertical and spatial variation when the optical contrast is isotropic), as a modulation in the reflected light in medium 1. This mapping has a limit of the vertical resolution of the height variation, which is determined by the detector sensitivity on capturing the corresponding modulation intensities.

From the instrumentation point-of-view, the setup consists of an optical microscope with an oil-immersion objective ( $NA = 1.25$ ) and an optical transducer. The transducer is a cover glass which can be attached either to the objective with a special collar or to the motorized microscope stage. In the latter case, a limiter protects the microscope objective from damage. The sample is placed on a motorized stage and it can be left at ambient atmospheric pressure and temperature. As for recording the image, a simple camera can be used for two-dimensional (2D) pictures and a three-axis oscilloscope for 3D pictures.

It is possible to image dielectric, metallic and *in vivo* biological samples with this technique, however, for the two latter, special conditions need to be fulfilled. Thus, the main advantage of this approach is to have real-time dielectric surface topography imaging, without scanning procedure. Reported lateral resolution was  $\sim 0.29\lambda$ , meanwhile without *PTM* the same setup achieved only  $0.4\lambda$ . Correspondingly, an axial resolution of  $\sim 0.75\lambda$  was shown.

### 3.1.1. Near-field scanning optical microscopy

The near-field scanning optical microscopy (*NSOM*) (also known as scanning near-field optical microscopy) is a technique that forms a bridge between scanning probe imaging and optical microscopy. The development of such an imaging method was motivated by the fact that far-field techniques are limited in resolution, meanwhile electron microscopes and tip-based scanning methods (e.g. *STM*, *AFM*) are suffering from poor performance in terms of resolving spectral (i.e. they are not optical methods) and dynamic properties (i.e. the long image acquisition time inhibits time-sensitive applications). The first description of the experimental scheme of the *NSOM* dates back to 1928 [48]. This early concept contained already all the necessary components of this imaging method, unfortunately it was only realized more than 50 years later [49–53]. New fabrication techniques, namely microtechnology-based processes developed in that era, allowed to create a subwavelength optical aperture at the apex of a sharply pointed transparent tip that was coated with metal. Furthermore, control electronics were available to maintain a constant gap width of a few nanometers between the tip and the sample, which was needed for scanning. The scanning configuration could be established in multiple ways, as is shown in Fig. 5. In the classical, aperture-based mode, the sample is placed on a hemispherical substrate and only a small area of it is illuminated [54,55]. The glass hemisphere acts a transducer and forwards the collected near-field information into the far-field, where the detectors are placed. Lateral resolutions between 10 and 100 nm were reported with this technique. In apertureless imaging mode (also known as tip-enhanced near-field optical microscopy (*TENOM*)) an external far-field illumination is strongly confined at the tip, which allows lateral resolutions down to 1–20 nm, but the signal must be extracted from the background noise generated by the aforementioned external light source [56–63]. During the third imaging mode, an uncoated dielectric tip is used to collect the near-field information in direct vicinity of the sample. This method is also called scanning tunneling optical microscopy (*STOM*) [64] or photon scanning tunneling microscopy (*PSTM*) [65].

The instrumentation governing the aperture-based *NSOM* imaging is relative simple, it consists of a single *laser* light source, piezo controllers for the tip, a motorized stage for sample positioning, optical elements to control the direction and the shape of the light and a detector. The most important parts of the setup are the microfabricated tip that determines the illumination reaching the sample and the objective that collects the light emerging from the sample. To maximize this collection, typically oil-immersion objectives with high  $NA$  ( $\sim 1.4$ ) are used.

For tip fabrication, two major methods were developed. The first approach is the so-called heating-and-pulling [66,67]. This is based on

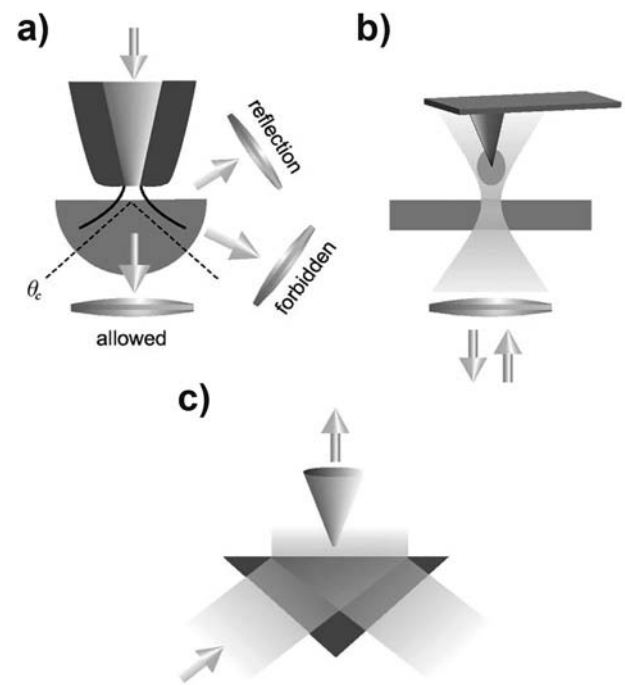


**Fig. 5.** Different imaging modes in *NSOM*. a) Aperture-based imaging with angular resolved detection. b) Apertureless imaging. c) Scanning tunneling imaging mode. Reprinted by permission from AIP Publishing: [5].

local heating with a carbon dioxide ( $CO_2$ ) *laser*, followed by a pulling of the glass fiber until the desired shape is reached. The advantage of this method is that it results in very smooth glass surfaces that are desired for effective metal evaporation. An important limitation of the process is the limited cone angle that is very difficult to increase above a certain level. The second approach is based on chemical etching with hydrofluoric acid (*HF*) [68,69]. The tip is first dipped into the *HF* that is covered with an organic solvent, then it is slowly pulled out. The result is an easily reproducible process that yields tunable cone angles. In early attempts this procedure led to bad surface roughness quality of the glass walls, but further improvements in the method overcame this issue [70]. Finally, both processes end with the same step. Aluminium is evaporated from below the tip that is held at an angle. This generates a shadowing effect at the tip and enables the self-aligned formation of the aperture.

The aperture of the tip has the highest influence on the performance of the imaging system. Its characteristic can be calculated with the Bethe-Bouwkamp model [71,72], since it gives a good approximation on the transmission coefficient. The value of this coefficient decreases for small apertures ( $<50$  nm) drastically, which makes the imaging almost impossible. A theoretical compensation would be the increment of the input power, but this would damage the metal coating of the tip. A good compromise between minimizing the aperture size and the input power simultaneously, is to set the diameter of the former to 80–100 nm. At this condition, the wavelength of the light becomes bigger than the opening on the tip, which results in an enhanced near-field power in the vicinity of the aperture. This plays a major role in the image formation, as was proven by several research papers [73–77]. These works also showed that scanning with constant gap between the tip and the sample is preferable due to the reduced number of artefact encounters.

The application range of the *NSOM* is widespread but restricted [5,78]. This is due to the fact that this imaging method offers super-resolution, furthermore, all the contrast mechanisms (e.g. absorption, phase and fluorescence) can be transferred more or less directly from conventional optical microscopy. However, compared to that a huge drawback is that only the surface of the samples can be imaged.



### 3.1.2. Tip-enhanced near-field optical microscopy

The tip-enhanced near-field optical microscopy *TENOM* is a special type of near-field optical techniques, where the *laser* light source illuminates a metal tip that is scanned over the surface of the sample. Super-resolution can be achieved, because the tip locally excites the sample and extracts the emitted light in parallel. The original method was published in 1985 [79], and since then, it evolved into three main branches: (i) scattering-type microscopy; (ii) tip-enhanced nonlinear optical frequency generation and mixing; (iii) tip-enhanced microscopy. In the first case, the sample response is detected in the far-field at the frequency of the incident light [80,81]. Special methods, like second-harmonic generation or four-wave mixing, belong to the second group [82–85]. The third branch utilizes locally enhanced fields to increase the spectroscopic response of the system [86–88]. The main governing phenomenon behind all the *TENOM*-based techniques is the field-enhancement that is generated at the metal tip. The three main contributors to this enhancement are the (i) electrostatic lightning-rod effect, (ii) surface plasmon resonances, and (iii) antenna resonances. All three of them can be tuned by adjusting the wavelength of the light, the shape, length and material of the tip and the surface features in the sub- or few-nanometer range. Furthermore, the field distribution and therefore the local enhancement also depends on the polarization of the light. Because of this, the exciting *laser* beam needs to be polarized along the tip axis [89]. Besides continuous excitation, short pulses also can be used for this type of imaging. The research field specialized on designing nano-optical fields with this method is called ultrafast nano-optics [90–93].

Although the previously discussed electric field is generated at the end of the tip, the optical signal (*i.e.* the image contrast formed during the scanning of the sample) does not simply reflect the tip shape. This is due to the fact that *TENOM* is not an *AFM* with optical information. On the one hand, the enhanced field causes an enhanced excitation rate that is contributing to an increase in the excitation density generated by the light source. On the other hand, the same field promotes the radiative decay. The theoretical background of these phenomena can be described based on the Purcell effect and Fermi's golden rule in the weak coupling range [94,95]. Based on this, it is possible to calculate the enhancement for both Raman scattering and fluorescence imaging modes. Since in the case of the former, the total signal depends on the product of the transition rates, the signal enhancement scales with the fourth power of the field enhancement, assuming that difference between the excitation and emission wavelength is small and field enhancement is not sensitive on these. As for fluorescence, the signal scales with the second power of the field, but it is also proportional to the ratio of the quantum yield of the tip and the sample. Because of the latter dependence, the most effective *TENOM* imaging was demonstrated with a sample of small quantum yield and high cycling rate [96,97].

The main instrumentation components of *TENOM* are very similar to those used in *AFM* or *STM*. For controlling the sample - gap distance, the same method can be used. The tip fabrication also relies on the same basis, but besides custom designs, nowadays a wide variety of tips are already commercially available. Three types of illumination can be applied, as shown in Fig. 6. For non-transparent samples, on-axis illumination is better, since this allows high *NA* objectives for imaging. In such a system, both Raman spectra and traditional imaging components (*e.g.* visible or near-infrared light detectors) are allowed in parallel. For non-transparent samples, side illumination fits better, because the polarization requirement of the tip antenna can be easily fulfilled. An alternative method is to use parabolic mirror objectives. They do not exhibit chromatic aberrations and they can be used at all temperatures, but their alignment accuracy is crucial since only minor deviations lead to undesired focal fields and therefore reduced detection sensitivity.

A big issue concerning *TENOM* is originated from the far-field illumination. The major problem with it that it is also collected by the detector, therefore the near-field signal has to compete with it (*i.e.* it has to

be enhanced to a level, where the *SNR* enables imaging). There are multiple techniques to reduce or eliminate the far-field background signal, one of them is the so-called tapping-mode imaging. This method induces an oscillatory movement of the tip, resulting in smaller and higher sample - gap distances. Using a demodulated optical signal and detection time tagging of the captured signals, even weak sources, like single fluorophores can be imaged. A different approach is to combine the aperture-based *NSOM* with *TENOM*. This results in the tip-on-aperture technique. Here, the evanescent waves created by the aperture are used for illumination for the tip-based imaging. A further advantage of this method is that the length of the tip can be fine tuned during fabrication, resulting a value that matches the antenna resonance, therefore realizing an extra enhancement. An alternative solution is to use surface plasmon propagation. This can be achieved through exciting a grating written into the tapered tip by focused ion beam. It is easy to see that, although *TENOM* can image with super-resolution [98], many restrictions must be met in order to enable this type of imaging.

### 3.2. Photon scanning tunneling microscope

Photon scanning tunneling microscopy (*PSTM*) (also known as *STOM*) is the third branch of *NSOM* [65]. Its working principle is analogous to the *STM*. An optical fiber probe tip is scanned over the sample surface, controlled by a feedback circuit that prevents collision of the two. However, the difference between the two microscopy systems is that, in the case of *PSTM*, the tip collects evanescent waves. These waves are generated as total internal reflection occurs when the light approaches from a higher *RI* medium to a lower one at a sufficiently high angle. The sample to be imaged is positioned on the total internal reflection surface in the second medium (*i.e.* the one with the lower *RI*). The tip of the optical fiber is also placed here, in a short distance from the interface, where the evanescent waves can be still collected. Due to the presence of the sample on the total internal reflection surface, a modulation in the evanescent waveforms will be present, manifesting itself as spatial variation in the field intensity. This can be recorded by the scanning tip, resulting in topological information about the sample.

The instrumentation of the *PSTM* consists of a *laser* light source, that is set at an angle, at which total internal reflection occurs at the edge of the first medium. Piezo-elements control the tip, just like in an *STM* setup. The tip might be coated, but it is not necessary for the operation. Shape and diameter of the aperture are critical for achieving super-resolution. Both of them can be tuned during the chemical etching process. The other end of the optical fiber is connected to a photomultiplier that serves as a detector during scanning. Acquired data must be processed by a computer in order to generate a gray-scale image of the sample.

Already during the first demonstration, *PSTM* achieved 200 nm lateral (with exciting wavelength  $\lambda = 633$  nm) and 80 nm axial resolution, meanwhile the noise level reached  $\sim 16$  nm peak-to-peak fluctuations. Although these results are not outstanding, it is important to note, that the theoretical resolution limit of this technique only depends on the effective sharpness of the tip. This statement was supported by a later-reported 10 nm lateral resolution [99].

### 3.3. Near-field optical random mapping nanoscopy

Near-field optical random mapping (*NORM*) nanoscopy was introduced in 2014 [100], and it combines the near-field acquisition with the far-field observation. The working principle behind this technique is to place objects in a scattering medium on the surface of the sample. Typically, these objects are nanoparticles. They can have different optical properties, such as transparency or reflectance, but their size must be smaller than the wavelength of the light. If this sole criteria is fulfilled, then it is possible to recover the near-field image from the far-field purely by determining the distribution of the scatterers (*i.e.* the



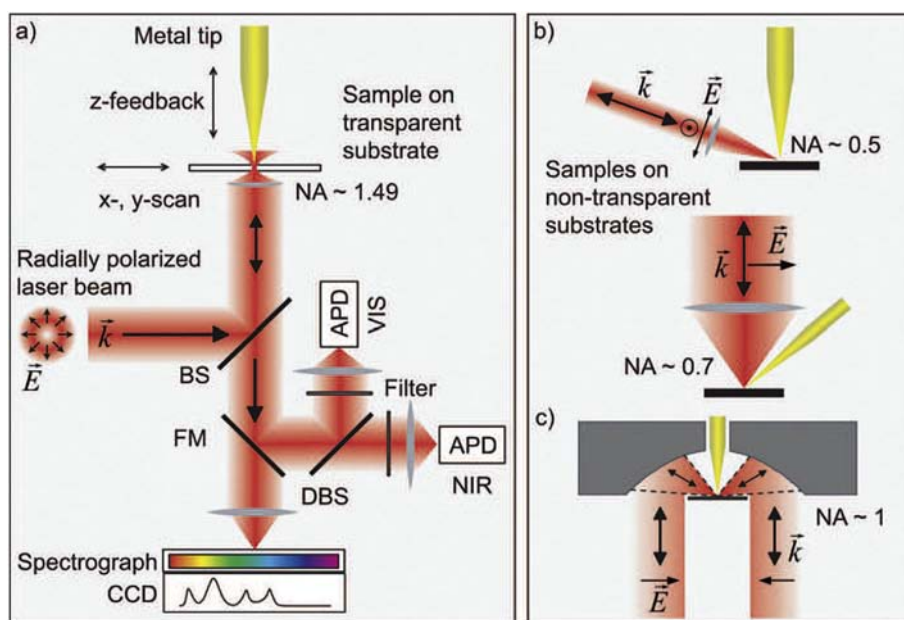


**Fig. 6.** Different illumination types in TENOM. a) On-axis illumination for transparent samples with both Raman scattering (spectrograph and CCD) and photoluminescence (avalanche photodiodes - APD and visible - VIS or near infrared - NIR spectral range) detection. b) Side illumination for non-transparent samples. c) Imaging with a parabolic mirror and high NA aperture. Reprinted by permission from Royal Society of Chemistry: [6].

nanoparticles). The method is very similar to the ones used for localization microscopies (see Section 2). Since the particles move stochastically due to the Brownian motion, their position can be determined with a much higher precision than the resolution of the far-field microscope objective. Additionally, the detected brightness of a single spot corresponds to the optical near-field intensity of the sample area below it. Therefore, observing the total sample area over time will provide information about all parts of the sample surface. However, a correction of the final image is needed, because the distance between the sample surface and the nanoparticles is not fixed. If the gap becomes too big, only low frequency spatial information will be transferred which will cause blurry picture. To dampen these lower frequencies, Fourier filtering can be applied on the final image.

To construct a NORM nanoscope, no special equipment is needed (see Fig. 7). The base of the setup is a standard optical microscope with a low-NA objective and a CCD camera. The recording speed of the camera (i.e. frames per second (FPS)) is the main factor that determines the image acquisition speed. Typical imaging times are between 1 and 10 min depending on the amount of pixels in the camera and its FPS rate. To improve the image quality dark-field illumination can be used that prevents non-scattered light from entering the objective. For successful imaging, a nanoparticle solution is also needed, as an example 120 nm titanium dioxide ( $\text{TiO}_2$ ) particles can be used, if the wavelength of the light is bigger than this dimension. In the same configuration, using 520 nm LED illumination, ~ 100 nm lateral resolution was reported [100]. This is a considerable improvement, because the same objective ( $\text{NA} = 0.4$ ) could only achieve ~ 650 nm resolution without the NORM system. However, there are two restrictions that must be met to be able to use this microscopy technique. The sample must not be sensitive on the nanoparticle solution and it must not be time-dependent, since the imaging takes up to several minutes.

Similarly to the far-field microscopy techniques, most of the near-field optical microscopy methods introduced in this section have already matured and commercialized in the past decades. Despite of their wide range of applications [5,6] (e.g. in imaging thin films, diffraction gratings or their application in fluorescent microscopy, near field Raman spectroscopy or pulsed laser ablation through their tips), they suffer from very low working distances, extremely shallow depth of fields, and long scan times for large sample areas.

#### 4. Micro-object-based super-resolution imaging

##### 4.1. Physics of the photonic nanojet

A new branch of super-resolution microscopy (SRM) started to emerge in 2004, when the first discovery of the PNJ-based resolution enhancement using high  $RI$ , dielectric-microobjects was published [101]. The PNJ is a very strong focused beam of light generated on the shadow side of a microobject (e.g. cylinder, semi-sphere, sphere), when illuminated by a plane wave. The length of this focus is  $\sim 2\lambda$  at FWHM, while its width is  $\sim 0.5 \pm 0.2\lambda$  at FWHM, depending on the parameters of the surrounding. The main influencing factors are (i) the refractive index of the medium ( $n_{\text{medium}}$ ), (ii) the diameter of the focusing curvature of the microobject/diameter of the microsphere ( $D$ ), (iii) the refractive index of the microsphere ( $n_{\text{sphere}}$ ) and (iv) the wavelength of the light ( $\lambda$ ). The exact mechanism of how these parameters influence the PNJ and how the PNJ enhances the resolution of the imaging, was studied extensively in the last decade and will be presented in the following paragraphs.

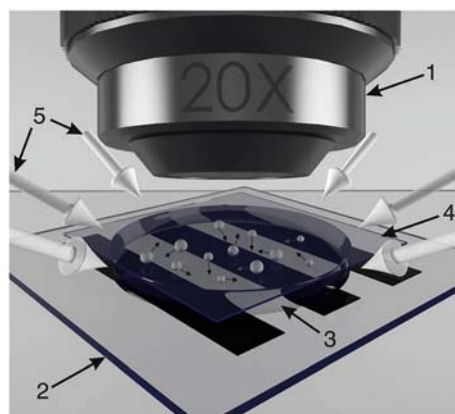


**Fig. 7.** Schematic of the NORM nanoscope. 1: microscope objective; 2: sample; 3: nanoparticle suspension; 4: cover glass; 5: incident light by dark-field illumination. Reprinted by permission from AIP Publishing: [100].

Imaging by a high  $RI$  lens, placed in vicinity of the sample, was demonstrated already in 1990 [102]. This technique was named solid immersion lens ( $SIL$ ) microscopy, because the sample had to be in close contact with the lens hemisphere in order to enhance resolution. An extra focus is created due to the geometrical shape of the lens that contributes to an effectively shorter wavelength and a decreased  $FoV$ , by a factor of  $\frac{1}{n_{SIL}}$  and to an increased magnification by a factor of  $n_{SIL}$ , where  $n_{SIL}$  is the  $RI$  of the  $SIL$ . However, to achieve this, the sample has to be in direct contact ( $\sim 0$  nm distance) with the lens. Theoretical calculations showed 15% increment in the width of the  $PSF$ , when this distance was increased to 100 nm. These calculations were made for  $n_{SIL} = 2.0$ ,  $\lambda = 546$  nm and a sample line-width of 100 nm. Experimental confirmation showed that this technique can be translated into practice, when a 100 nm lines-and-spaces pattern ( $LSP$ ) was imaged.

The  $LSP$ -s are typical samples that are used to measure the spatial frequency response of an optical system. They consist of parallel, equidistant lines with a given width. The spacing distance between them is the same as the line-width, unless in uniquely specified cases. The lines and the spaces have big contrast difference, ideally, one part generates a totally white, the other a totally black signal. Therefore, the intensity profile of this pattern is a rectangular function. To characterize the performance of an optical system in terms of contrast and resolution, its response can be measured and compared to this reference.

The advantages of the  $SIL$ -based system are its simple construction and a performance depending almost entirely on the  $RI$  of the applied lens. However, to improve its performance,  $n_{SIL}$  has to be increased, which cannot be done infinitely due to material properties. Alternatively, the wavelength of the illumination can be decreased, but again, that is restricted to the spectrum of the visible light. Moreover, the  $FoV$  is also limited. This could be overcome by implementing a scanning procedure [102], but that would disable the imaging of time-sensitive samples.

An alternative solution of using materials with negative  $RI$  was proposed in 2000 [103]. In this work a theoretical approach is shown to amplify the evanescent waves and transfer the information coded in them into the far-field. The major concern regarding this technique is that it is restricted to a certain frequency and to special materials of both the lens and the medium.

Discovery of the  $PNJ$  enhancement opened up a new development direction in microscopy [101]. It was shown by finite-difference time-domain ( $FDTD$ ) numeric simulations, that dielectric  $\mu S$ -s can generate this special type of light focusing, when they are placed in a medium with tuned  $RI$  (Fig. 8). More importantly, it was pointed out that, if a sample (e.g. a nanoparticle) is placed in this  $PNJ$ , the generated backscattered light is increased multiple folds, therefore its detection became possible. This effect is the basis of the microobject-based super-resolution imaging. Further investigation using a generalized multiparticle Mie method showed that the  $PNJ$  formation and the enhanced backscattering are also present in 3D [105,106]. These results started further investigations concerning the physical phenomena behind the light focusing and backscattering.

Already in 2005, the  $PNJ$  formation was precisely described by the combination of geometrical optics, Mie theory and angular spectrum analysis [107]. This theoretical investigation calculated the field structure with Mie theory, then resolved and translated the Mie solution into a Debye series. Finally, it obtained and analysed spatial characteristics of the  $PNJ$ . Results showed that the jet formation is possible because of a unique combination of (i) a peak in the angular spectrum, (ii) the finite content of the propagating spatial frequencies, (iii) a small but also finite content of the evanescent spatial frequencies and (iv) a special distribution of the phase. Furthermore, it confirmed the four main influencing components of the  $PNJ$ , detailed in the beginning of Section 4. These findings were later supplemented by a study about the 3D spectral analysis of the  $PNJ$  [108]. Here, the contribution from all spatial frequencies was investigated. Based on the performed

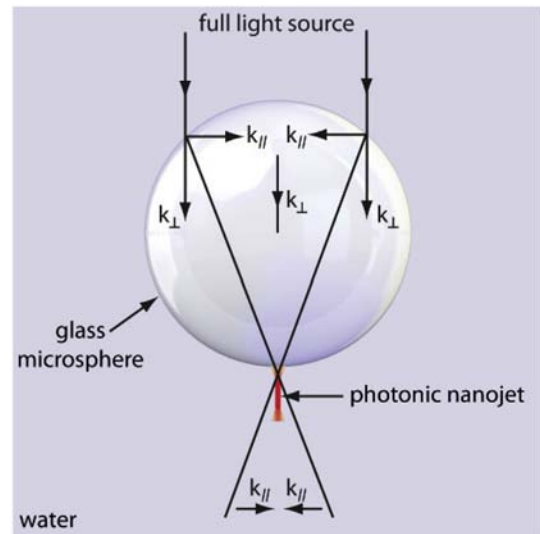


**Fig. 8.** Concept of the  $PNJ$  generation. When the microsphere is illuminated by a full light source, the left and right wave-vectors  $k_{\parallel}$  are cancelling each other, while the  $k_{\perp}$  wave vectors are superimposed. Interference of the optical fields therefore can generate the nanojet with confined transverse beam width and extended longitudinal beam length. Reprinted with permission from [104]. Copyright 2016 American Chemical Society.

decomposition, it is clear that mainly propagating waves are contributing, but the presence of the evanescent components close to the  $\mu S$  surface is crucial. Because the generation of the latter waves depends also on the  $RI$  mismatch on the border of the  $\mu S$  and the medium, changing any of those materials highly affects the shape and the strength (i.e. the field gradient) of the  $PNJ$ . These pioneering theoretical works gave an insight into the physics of  $\mu S$ -focused illumination light even before the first experimental confirmation of the phenomenon was published.

Parallel to these studies, the enhancement of the backscattered light was also investigated [109]. The enhancement of the backscattering, originating from the  $PNJ$  illuminated nanoparticles, was characterized. It was shown, that the enhancement is due to a complex interaction between the  $\mu S$  and the imaged nanospheres, furthermore, the scaling factor is proportional to the third power of the size of the latter. This complex interaction can be considered as a feedback system. The nanoparticle is excited by the  $PNJ$  and therefore its scattering intensity is elevated proportionally to the intensity of the  $PNJ$  ( $\sim 2$  orders of magnitude in the investigated case). This causes a backscattering in the fields and changes the normal electromagnetic modes of the  $\mu S$ . As this process is constructive, it elevates the backscattering intensity further with around 4–9 additional orders. The highly elevated intensity is directly responsible for the enhanced imaging and enables super-resolution.

#### 4.2. Experimental evidences for the photonic nanojet

The experimental confirmation of the existence of the  $PNJ$  was demonstrated in 2008 [110]. Latex  $\mu S$ -s of 1, 3 and 5  $\mu m$  diameter were deposited on a cover glass in low concentration to avoid cross-scattering and they were imaged in air and water-immersion, respectively. To be able to map the shape of the expected  $PNJ$ , a laser scanning confocal microscope with an avalanche photodiode was used for signal acquisition. Collimated, unpolarized white light was applied to the sample, but a band pass filter (500–540 nm) was placed in front of the detector. Image stacks with 500 nm steps of focus were captured within  $\sim 400$  s, which was followed by data processing. Final pictures served as a proof for the existence of the  $PNJ$ -s. It was also demonstrated that multiple  $\mu S$ -s can produce  $PNJ$  simultaneously, without interference. Therefore, this study proved that  $\mu S$ -based SRM is a viable alternative microscopy technique.

The research of *PNJ*-s and their application in microscopy techniques started to bloom around 2010. Numerous papers were published about the modification of the shape and the size of the *PNJ* [112]. As an example, it was shown by numerical experiments, that it is possible to confine the *PNJ* when illuminating the  $\mu\text{S}$  with a tightly focused Gaussian beam through a high-*NA* objective [113]. The concluded cause of this shrinkage was the interference of the electric field and the collimation of the incident field, both caused by the  $\mu\text{S}$ . Although this model had some limitations (e.g. only dielectric materials were used and the resonance phenomenon was omitted), it showed the possible application of fluorescent signal detection. An alternative way of tuning the shape of the *PNJ* was demonstrated by constructing two-layer  $\mu\text{S}$ -s [114]. Calculations revealed, that the 'waist' (i.e. the width at *FWHM*) of the *PNJ* can remain smaller than the wavelength of the light independently from the diameter of the  $\mu\text{S}$  if the optical contrast (i.e. the ratio between  $n_{\text{sphere}}$  and  $n_{\text{medium}}$ ) is tuned optimally. However, since this tuning is restricted in the number of possible combinations (e.g. its upper boundary is  $\sim 1.7$ ), this sets a limitation on possible *D* values. Furthermore, considering a two-layer  $\mu\text{S}$  with precisely chosen refractive indices for both the core and the shell of it, it is possible either to significantly elongate the length of the *PNJ* or to highly increase its peak intensity. The former modification could be the basis of a nanometer-sized inhomogeneity detection technique [115].

Parallel to the computational studies, experimental approaches were also developed. It was shown that not only  $\mu\text{S}$ -s, but hemispheres are also able to create a *PNJ* and that they can be used for imaging [116,117]. For demonstration, 0.05–3  $\mu\text{m}$  diameter hemispheres were grown and randomly placed on the sample surface. Imaging was performed in both orientation (i.e. with the flat and the curved surface of the hemisphere facing down). The magnifying effect and the resolution enhancement was measured on *LSP*-s. Published pictures confirmed a magnification factor of  $\sim 1.6$ . In contrast, the exact value of the resolution enhancement could not be easily determined, because the study focused more on the fabrication technology than the quantification of the resolution enhancement. Despite of this, since the resolution limit ( $\sim 262$  nm, when calculating Abbe's limit) of the imaging system used for the experiment was very close to the pitch of the imaged *LSP*-s (220–250 nm), the achieved improvement could not be more than  $\sim 15\%$ . A more concerning issue about this microscopy technique originates from the fact that the *FoV* is limited by the diameter of the applied hemisphere and the location of this hemisphere is arbitrary and cannot be controlled. Therefore, in order to move it in any desired location, a manipulator system must be employed.

Utilizing the  $\mu\text{S}$ -s for single-molecule imaging was found to allow high-temperature imaging and to simultaneously improve photostability [118]. Coated  $\text{TiO}_2$  spheres ( $D = 2$   $\mu\text{m}$ ) were coupled to the sample by Cy3-labelled streptavidin for this experiment series. Results showed that the lifetime of the fluorophore before bleaching was increased in the presence of the  $\mu\text{S}$ , meanwhile molecular activity (e.g. DNA polymerase activity) could have been observed. A further advantage of this technique was the capability of allowing sample temperatures as high as 70 °C.

One of the first reports demonstrating the true potential of the  $\mu\text{S}$ -based super-resolution imaging in the field of wide-field microscopy was published in 2011 [111]. In this study, silicon dioxide ( $\text{SiO}_2$ ) ( $2$   $\mu\text{m} < D < 9$   $\mu\text{m}$ ) were spread in a single layer over the surface of the sample and illuminated by white light ( $400$  nm  $< \lambda < 700$  nm, with peak at  $\lambda = 600$  nm). The imaging system, called (white-light) optical nanoscopy (*ON*) could be operated both in transmission (Fig. 9a) and in reflection (Fig. 9b–d) mode. For acquisition, the objective was not focused to the sample-plane, but  $\sim D/2$  distance below. That is, where an enlarged virtual image of the sample is formed by the  $\mu\text{S}$ -s. This virtual image was recorded by a microscope-mounted camera. The performance of the *ON* was evaluated by measuring multiple patterns using

an objective with  $NA = 0.9$ . This resulted in an Abbe's resolution limit of  $\sim 222$  nm. As reference, scanning electron microscopy (*SEM*) pictures were taken. First, the surface of a Blu-ray disc [119] without its protective film was imaged, and the *ON* could resolve its *LSP*. The pitch of this pattern was 300 nm that is above the resolution limit. A similar situation was presented next, when another *LSP* with 490 nm pitch was imaged. In the third case, a gold-coated anodic aluminium oxide membrane was investigated. This structure had a fishnet pattern with a pitch of  $\sim 100$  nm that is considerably below the diffraction limit. Still, the *ON* could resolve this pattern. However, the authors admitted, that the special surface (i.e. the gold coating) caused a near-field interaction that helped the resolution enhancement. Despite of that, super-resolution imaging was clearly demonstrated. More importantly, it was pointed out, that the performance of  $\mu\text{S}$ -based microscopy may depend on the sample.

In the same year, an extensive experimental study was carried out about the influence of the illumination on the *PNJ* [120]. A high-resolution interference microscope was employed to enable precise measurement of both the amplitude and the phase of the *PNJ*-s. As a general observation, it was stated that the physical optics effects largely dominate the properties of the *PNJ*-s, therefore, their behaviour can be understood by applying conventional refractive optical arguments. First, the dependency on the wavelength of the light was confirmed by measuring the changes generated by switching the illumination between three lasers with different wavelengths. It was found that the shape, the size and the position can be changed by varying  $\lambda$ , but the *PNJ* is always close to the surface of the  $\mu\text{S}$ . Important to note is that  $D = 2$   $\mu\text{m}$  glass spheres ( $n_{\text{sphere}} = 1.55$ ) were measured. To adjust this position further away from the surface of the  $\mu\text{S}$ , spherical wavefronts of the illumination with various radii were proposed. These can relocate the *PNJ* up to several microns away, however, at a cost of slightly larger spot size. It was also demonstrated that it is possible to generate a two-spot *PNJ* by applying an off-axis Bessel-Gauss beam as illumination. In such a scenario, 200 distance between the two *PNJ* was observed with  $\lambda = 642$  nm, which results in a spot size below the diffraction limit of the highest *NA* microscope objectives. To prove the first general statement of the study, other unique shapes (e.g. doughnut shape or two half-circles shape) were shown by applying different polarization-induced illumination beam shapes. Through this demonstration, it was proven that the *PNJ* is an optical phenomenon that can be also fine-tuned for wide range of applications by adjusting the properties of the illumination.

A similar study was conducted also on glass *SIL*-s [121]. Here,  $\text{SiO}_2$  hemispheres ( $D = 2$   $\mu\text{m}$ ) were microfabricated and characterized. The measurement method was matching the one described in the previous paragraph. Results showed that spot size reduction was also present when illuminating hemispheres and its extent was in good agreement with the theoretical value calculated for  $\text{SiO}_2$   $\mu\text{S}$ -s. Furthermore, a  $\sim 50\%$  peak intensity increment was measured, compared to the illumination without the *SIL*. Transmission loss through the hemispheres was also investigated and found to be  $\sim 17\%$ , which was categorized as a sufficiently small value for applications (e.g. optical trapping). An indirect conclusion of this work was to show that the illumination pattern can be transferred to the *PNJ*-s independently from the shape of the microobject transducer [122]. As an alternative to glass lenses, polymer hemisphere fabrication was demonstrated in the same year [123]. The main advantage of using photocurable polymer droplets was the easy shape control. During the process, the lenses were created on a poly (dimethylsiloxane) (*PDMS*) stamp that was used to transfer the droplets to the final substrate. The only constrain regarding the target material was its surface roughness, which had to be moderate. A further advantage of the technique was the option for stamp-geometry-dependent, high-density array fabrication. However, the need of further material optimization was reported in order to be able to generate high contact angle lenses on various surfaces.



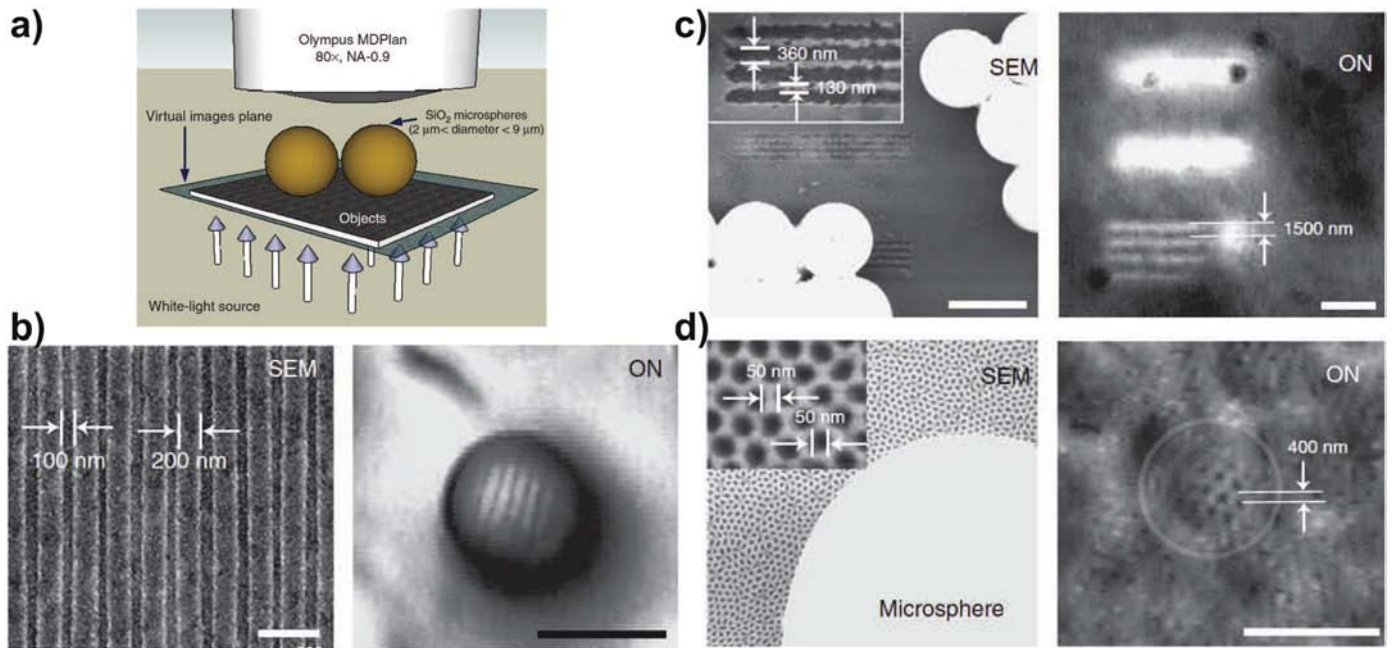


**Fig. 9.** The ON. a) Schematic of the experimental configuration of the white-light nanoscope, operating in transmission mode. b) Parallel lines from the surface of a Blu-ray disc, as imaged by SEM (left) and the ON in reflection mode (right). The protective film was removed from the disc before imaging. Scale bar: 500 nm for SEM and 5 μm for ON. c) Image of a LSP with increased gaps, taken by SEM (left) and ON (right). The white, circular objects on the left are the μS-s, placed on the surface of the sample. Scale bars: 5 μm. d) Photograph of a gold-coated anodic aluminium oxide membrane, taken by SEM (left) and ON (right). Scale bars: 5 μm. Reprinted by permission from Springer Nature: [111].

#### 4.3. Towards larger dielectric micro-objects for increased field-of-view imaging

At the dawn of microobject-based SRM, only μS-s and hemispheres smaller than 10 μm were considered for imaging. However, it is possible to use spheres up to 200 μm for super-resolution imaging, as was shown in 2012 [124]. Barium titanate glass (BTG) μS-s ( $2 \mu\text{m} < D < 200 \mu\text{m}$ ,  $n_{\text{sphere}} \sim 1.9\text{--}2.1$ ) were immersed in water ( $n_{\text{medium}} = 1.33$ ) and isopropyl alcohol (IPA) ( $n_{\text{medium}} = 1.37$ ), respectively, for demonstration. The microscope used for acquisition was equipped with a 100×, NA = 0.9 objective. Illumination originating from a halogen light source was filtered to  $550 \pm 10 \text{ nm}$ . The imaged sample consisted of an array of gold cylinder pairs with 120 nm diameter each and the same distance between the members of a pair. The height of each cylinder was 30 nm, composed from 2 nm of chromium and 28 nm of gold. The μS-s were placed randomly on the sample and covered with IPA. Then a μS was found that was located directly above a pair of the gold cylinders. For imaging, the microscope objective was focused to the virtual image plane, located  $\sim D/2$  below the sample plane. Resulting images and their analysis for various μS diameters are shown on Fig. 10. Plotting the intensity along the marked measurement lines showed, that the signals generated by the two cylinders can be separated. Control images revealed, that these patterns cannot be resolved solely by the microscope objective. Calculating the resolution improvement showed that originally this was  $d = 306 \pm 6 \text{ nm}$ , while the μS-s resolved a pitch of 240 nm. The latter can be calculated somewhat smaller considering the FWHM instead of the peak-to-peak distance. However, as it was mentioned earlier [111], the near-field interactions between the gold surface and the μS might further improve the imaging resolution, therefore the presented increment is sample-dependent. Measuring μS-s with various diameter showed that increasing  $D$  increased linearly the FoV. However, the biggest magnification was not found with the smallest μS but when  $6 \mu\text{m} < D < 10 \mu\text{m}$ . This work successfully presented the possible application of μS-s bigger than 10 μm diameter for imaging. Repeating the experiments under water-immersion also proved the applicability of the method for imaging biological samples.

By the time of 2013, the field of μS-based SRM was widely expanded and three main directions of development became distinguishable: (i) further exploring the PNJ; (ii) demonstrating the imaging capabilities of various μS-s; (iii) finding new solutions to extend the FoV of μS-based imaging systems.

Since larger diameter μS-s were already investigated and their PNJ creating abilities recognized, the research spotlight turned towards smaller spheres, particularly, to the case, when  $D$  becomes comparable

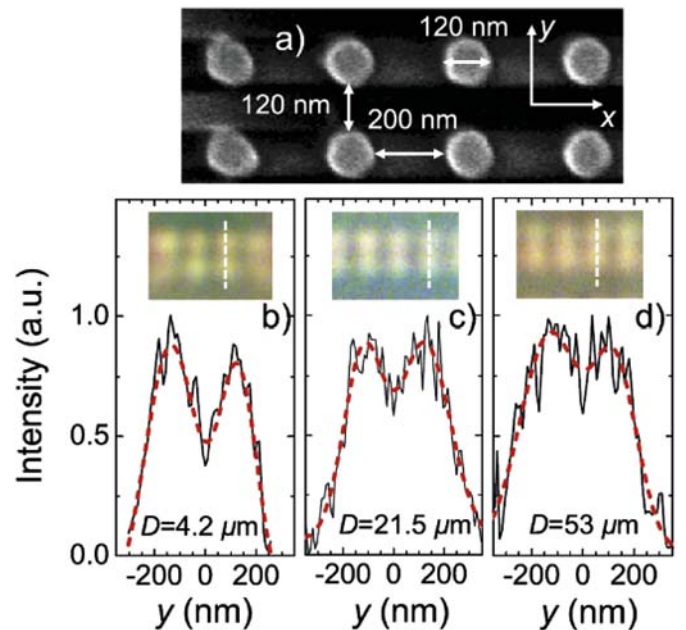


**Fig. 10.** Super-resolution imaging with BTG μS-s. a) SEM picture of gold nano-cylinders, serving as the sample to be imaged. Pictures taken through b)  $D = 4.2 \mu\text{m}$ , c)  $D = 21.5 \mu\text{m}$ , d)  $D = 53 \mu\text{m}$  BTG μS-s, with their intensity profiles along the marked measurement lines, respectively. Black lines correspond to raw data, while red dashed-lines represent a Gaussian fit of the intensity plots. Reprinted by permission from AIP Publishing: [124].



to  $\lambda$  [125]. It was shown theoretically, that high  $RI$   $\mu S$ -s at Mie resonances can significantly increase the field around them (*i.e.* generate a strong  $PNJ$ ). The model explicitly showed a non-monotonic dependence of the resolution on the wavelength, confirming the enhancement due to the resonances. This special feature could be exploited while imaging broadband point emitters such as dye molecules or fluorophores. However, several practical problems were raised in connection with this technique. Mainly, it is particularly difficult to handle such small  $\mu S$ -s. This could hinder experimentation, as without precise positioning the desired part of the sample cannot be imaged directly. Moreover, the created  $PNJ$ -s are very close (in the range of  $\lambda$ ) to the  $\mu S$  surfaces. This latter issue was overcome by introducing two-layer  $\mu S$ -s that could project  $PNJ$ -s up to  $\sim 4\lambda$  distance [126]. The special composition of such gold- $SiO_2$   $\mu S$ -s allowed working distances comparable to the regular ones ( $10\ \mu m < D$ ). The long- $PNJ$  projecting property of the core-shell type  $\mu S$ -s were also exploited for bigger diameters [127]. When illuminating a  $D = 5\lambda$ , two-layer  $\mu S$  ( $n_{sphere} = 1.6028$  and  $n_{shell} = 1.8445$  for the inner and the outer layer, respectively), the measured length of the generated  $PNJ$  was  $\sim 22\lambda$ . For comparison, a single layer  $\mu S$  ( $n_{sphere} = 1.377$ ) with the same diameter could achieve only  $\sim 9\lambda$  length. In both cases, the illumination wavelength and the refractive index of the medium was kept the same. A further iteration on this technique was shown when the core of the two-layer structure was removed and the generated hollow structure was filled with liquid [128]. This theoretical investigation showed that by fine-tuning the  $RI$ -s of the medium and the liquid within the  $\mu S$ , the  $PNJ$  can be elongated over  $100\lambda$  distances.

Parallel to the investigations on the double layer  $\mu S$ -s, other unconventional geometries were investigated for their potential applicability on  $PNJ$  generation. One of them was a study on elliptical particles [129], and simulations predicted, that  $PNJ$ -s still could emerge. These results gave an additional degree of freedom for designing optical systems utilizing  $PNJ$ -s. Another theoretical study on various geometries focused on the influence of the surface roughness [130]. Three cases were modelled: (i) a completely smooth surface, (ii) a surface with regular pattern and (iii) a surface with random pattern. Interestingly, the first two  $\mu S$ -s could produce  $PNJ$ -s both in air and in water medium, meanwhile the one with the random roughness could only generate it in air. These results showed, that although the surface roughness is an important parameter, the  $RI$  of the medium may have a bigger impact on the final formation of the  $PNJ$ . As an extensive review showed in 2017 [8], the  $PNJ$  became a well-recognized phenomenon in optics. By that time, almost all the influencing parameters, structures and geometries were investigated theoretically and most of them also confirmed experimentally. Knowledge about these influencing factors gave the researchers a relatively large freedom in designing optical systems, however no conclusive design principle was laid down so far that would allow the accurate prediction of the final performance of a micro-object-based microscopy system in terms of achievable resolution gain.

The second development direction focused on demonstrating the imaging capabilities of various  $\mu S$ -s in multiple conditions. A study showing a possible way to increase the  $FoV$  of a  $\mu S$ -based microscopy system was shown in 2013 [131]. Their method consisted of observing the sample in air, through big diameter (30, 50 and  $100\ \mu m$ ) polystyrene  $\mu S$ -s ( $n_{sphere} = 1.59$ ) that were placed on the top of it. For the image acquisition, a halogen light source and a  $50\times$ ,  $NA = 0.75$  objective was used. Pictures, taken from two different samples were shown. One of them was the surface of a Blu-ray disc (without the protection film), while the other was a quartz plate with gold nanopatterns. The 300 nm pitches (180 nm lines with 120 nm spaces) of the Blu-ray disc were resolvable in the presence of all the differently-sized  $\mu S$ -s. The same results were obtained when the 150 nm gold nanoparticles with 600 nm spacing on the quartz plate were imaged. Since the authors did not mention any applied filtering, the resolution of the microscope without the  $\mu S$ -s could only be estimated. Considering the lower end of the visible light spectrum ( $\lambda = 400\ nm$ ), possible limits are  $\sim$

267 nm according to Abbe's law or  $\sim 325\ nm$  according to Rayleigh criterion. Based on these assumptions, the achieved extra resolution is minimal in the case of the Blu-ray disc imaging. As for the gold nanoparticles, there the gold surface adds an uncertainty factor in the estimation of the purely  $\mu S$ -based enhancement. Moreover, the huge pitch (compared to the diffraction limited feature size) further reduces the detection limit.

It was demonstrated in the same year, that water-immersion imaging in a similar configuration is possible. The  $BTG\ \mu S$ -s ( $D = 100\ \mu m$ ,  $n_{sphere} = 1.9$ ) were placed on the sample, which was a cluster of adenoviruses in the presented case. The typical size of such a virus is  $\sim 75$ – $100\ nm$ . Indeed, analysis of the intensity values on the recorded images showed, that the individual viruses were resolved. Therefore, it was proven that biological samples can be imaged with  $\mu S$ -based SRM.

A study, comparing the performance of the  $SIL$ -s with the  $\mu S$ -s showed superior performance of the latter [132]. This was concluded after the same sample (gold nanocylinders with 100 nm diameter and 160 nm pitch) was imaged by the two different methods under the same conditions (see Fig. 11). In both cases a  $20\times$ ,  $NA = 0.6$  objective with  $\lambda = 405\ nm$  illumination was used. The refractive indices were almost identical ( $n_{sphere} \sim 1.9$  for the  $BTG\ \mu S$  and  $n_{SIL} \sim 2$  for the  $SIL$ ), but the diameter of the  $\mu S$  was five times bigger ( $D = 10\ \mu m$ ) than the diameter of the  $SIL$  ( $D_{SIL} = 2\ \mu m$ ). Other parameters (*e.g.* magnification factor) were also investigated, which showed, that both in terms of resolution and magnification, the  $\mu S$ -s can provide higher performance. These findings induced further research on potential  $\mu S$ -based microscopy applications.

It was also shown that  $\mu S$ -s can also be combined with scanning laser confocal microscopes [133]. To merge the two technologies, researchers followed a very simple method. They placed the  $\mu S$ -s at random locations on the top of the sample by mixing them into a solution and then pouring it on the surface. After evaporating the liquid component, the sample was imaged by the confocal microscope utilizing a laser light source with  $\lambda = 408\ nm$ . In this demonstration (Fig. 12), an anodic aluminium oxide template with 25 nm holes and 50 nm pitches was used. To be able to measure the resolution enhancement produced exclusively by the  $\mu S$ -s (fused silica with  $D = 2.5, 5, 7.5\ \mu m$ ,  $n_{sphere} = 1.47$  and polystyrene  $D = 5\ \mu m$ ,  $n_{sphere} = 1.62$ ), the surface was not coated with gold. Acquired photographs showed that the sample patterns were resolved. Unfortunately, the authors did not provide any intensity or modulation measurement data for these experiments, therefore comparison with other methods and exact resolution calculations are difficult to make. Moreover, it is important to note, that these

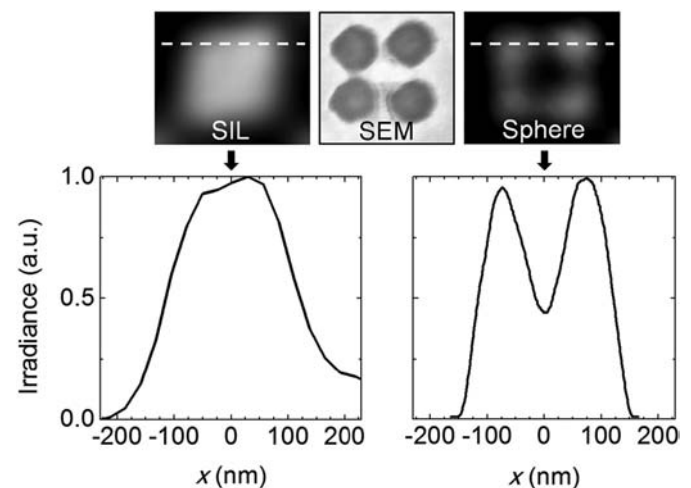


**Fig. 11.** Comparison of the imaging performance of a  $SIL$  against a  $\mu S$ . The same nanopattern (center, SEM image) was imaged by a  $SIL$  (left) and by a  $\mu S$  (right). Corresponding analysis of the detected signals along the measurement lines are plotted below, respectively. Reprinted by permission from AIP Publishing: [132].

impressively low-dimensional features were imaged with a *laser* light source that provides increased illumination power and reflected light intensity. Another non-negligible factor is the confocal setup that by itself provides an increased resolution compared to a classical optical microscope due to the engineered *PSF*.

Following the idea of potential applications of high-*RI*  $\mu$ S-s [124], biological sample imaging with a similar setup was demonstrated in 2014 [134]. Here, super-resolved features of sub-cellular organelles and biomolecules were shown both in water- and oil-immersion with  $40\times$ ,  $NA = 0.8$  and  $63\times$ ,  $NA = 1.4$  objectives, respectively. Proving the imaging capabilities of  $D = 60\mu\text{m}$  BTG  $\mu$ S-s in these conditions confirmed their applicability for life science-related microscopy. These findings were reproduced in the following year, when the same  $\mu$ S-s were embedded in PDMS and used for imaging various biological samples including mouse kidney tissues, proteins and human glioblastoma cells in both wide-field and fluorescent mode [135–137]. The advantage of the elastomer fixation was that the fabrication process could be done independent of the experiments. Furthermore, since no immersion liquid was needed, inverted microscopes could be used too and the potential effect of evaporation of the immersion medium was avoided. However, as it was pointed out in a follow-up paper [138], two issues may hinder this kind of experimental approach. The *FoV* is limited by the diameter of the  $\mu$ S despite of the thin-film approach. Various techniques overcoming this issue, including the one shown in [138] will be presented in the following paragraphs. The other concern is the practical handling of the PDMS films as they can be difficult to peel off from the substrate depending on their thickness. To assist the experimentation, the placement of a transparent tape on the substrate was proposed. The tape could reduce the surface energy and the Young's modulus effectively, therefore enabled the peeling without damaging the film. The thickness

of the PDMS layer was regulated during the spin-coating of the uncured polymer. Measurements for PDMS films with  $\sim 3\text{--}100\mu\text{m}$  thickness showed its effect on both the achieved magnification and the *FoV*. The former was found to be decreasing when layer-thickness was increased, while the latter had a maximum at  $\sim 10\mu\text{m}$  thickness. These values were found for BTG  $\mu$ S-s with  $D = 15$  and  $20\mu\text{m}$ . In those cases, when the diameter of the sphere was higher than the PDMS-layer, the surface of the  $\mu$ S-s was covered evenly with the given thickness of PDMS.

Besides for biological applications, the  $\mu$ S-based SRM could be also applied in the field of metrology [139]. Since diffraction-limited feature sizes are common in modern electronics, a general need for observation and optical investigation was raised. The most common method for imaging is currently the SEM. However, its instrumentation is expensive, sensitive to vibrations and its not optimal for imaging non-conductive samples. Both of these issues could be avoided by imaging with dielectric  $\mu$ S. In the presented paper,  $D = 60\mu\text{m}$  BTG  $\mu$ S-s were proposed for imaging. As a demonstration, a silicon template with LSP-s was observed. It had  $220\text{ nm}$  pitch with non-equal line and space widths, since the lines were  $120\text{ nm}$  wide. The microscope used for these experiments was equipped with a halogen light source ( $400\text{ nm} < \lambda < 750\text{ nm}$ ) and a  $63\times$ ,  $NA = 1.4$  objective. This resulted in a diffraction limit of  $d = 174\text{ nm}$  (Rayleigh criterion) or  $d = 143\text{ nm}$  (Abbe's law). The authors claimed to resolve this pattern with the help of the  $\mu$ S-s, but not with the microscope alone. This causes a contradiction, because the pitch of the LSP was  $220\text{ nm}$ , therefore the microscope also should have been able to resolve it. Unfortunately, no measured intensity data or modulation supporting the images were published, therefore the cause of the difference is not obvious. However, it is possible that without the extra  $\sim 2.8$  magnification factor produced by the  $\mu$ S-s (measured data), the microscope-mounted camera was not able to map the

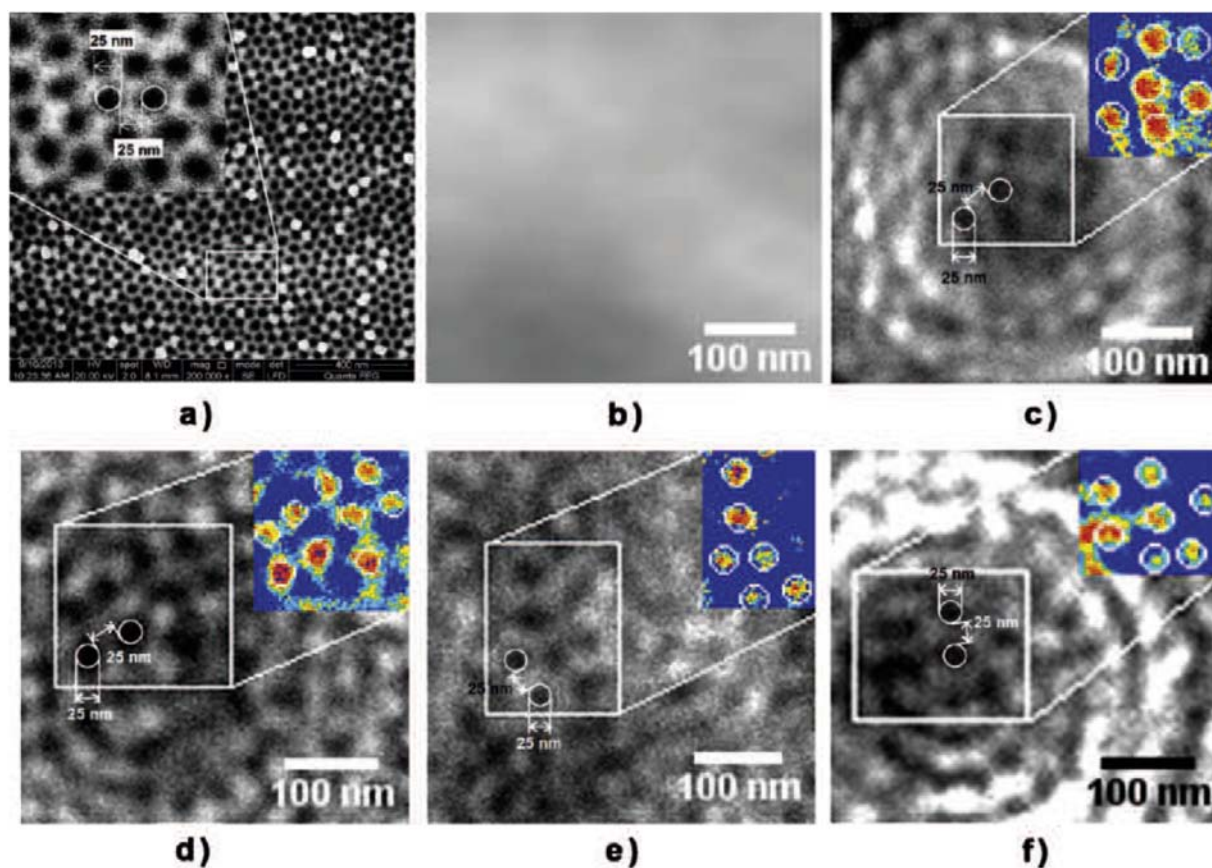


**Fig. 12.**  $\mu$ S-based super-resolution imaging with a scanning *laser* confocal microscope. Images of an anodic aluminium oxide template with  $25\text{ nm}$  holes and pitches imaged by a) a SEM b) a scanning *laser* confocal microscope in combination with c)  $5\mu\text{m}$  fused silica  $\mu$ S, d)  $2.5\mu\text{m}$  fused silica  $\mu$ S, e)  $7.5\mu\text{m}$  fused silica  $\mu$ S and f)  $5\mu\text{m}$  polystyrene  $\mu$ S. Insets show the corresponding pseudocolor images. Reprinted with permission from [133]. Copyright 2014 American Chemical Society.

structure properly, due to its pixel-size limitation, causing too small modulation in the final image for the human eye to detect.

A novel approach on microobject-based SRM was reported in 2016 [140]. By assembling 15 nm  $\text{TiO}_2$  nanoparticles, a 3D dielectric metamaterial was constructed. This could be placed on various samples for imaging, similarly to a SIL. The metamaterial could create an array of illumination spots on the sample surface (like a  $\mu\text{S}$ ) and simultaneously could couple the near-field information into the far-field. To demonstrate this effect, various geometrical patterns from a semiconductor wafer with gold-coated feature sizes down to 45 nm were imaged. The main optical components besides the metamaterial-SIL consisted of a classical optical microscope with  $100\times$ ,  $\text{NA} = 0.8$  objective and a CCD camera. The sample was imaged in three illumination conditions: white light (full visible spectrum), green light ( $\lambda \sim 540$  nm) and blue light ( $\lambda \sim 470$  nm). The pattern was recognizable in all cases, however, no intensity or modulation analysis was provided with respect to the photographs. Although this system provides one of the best resolutions within the microobject-based SRM techniques, again, the smallest detectable features were demonstrated on a gold-coated surface that induces uncertainty in the performance analysis. Moreover, the preparation and handling of the assembled  $\text{TiO}_2$  spheres were not so straightforward as other previously shown  $\mu\text{S}$ -based methods.

Another microscopy system demonstrating super-resolution imaging was reported in the same year [141]. Here, BTG  $\mu\text{S}$ -s were placed in a commercial white light interferometer. The unique choice of hosting environment enabled to construct 3D images when scanning the sample with the help of a piezoelectric translator. Results showed, that the same topography resolution could be achieved as with an AFM, but because in the x-y plane the FoV was extended by the  $\mu\text{S}$ , the scanning time could be significantly reduced. The lateral resolution of the system was determined using water-immersed  $\mu\text{S}$ -s. Various silicon-based samples were imaged and diffraction-limited features were resolved. The authors claimed 50 nm lateral and 10 nm axial resolution, however the former was stated based on detecting a feature with that size and a much greater pitch. As they concluded in their work, the main advantage of this 3D super-resolution technique is the reduced scanning time compared to an AFM.

Many  $\mu\text{S}$ -based imaging techniques were shown so far with various approaches and results. But, as it was pointed out, the main issue with most of them is that their resolution measurement method is arbitrary. Although claims of the fundamental limit of  $\mu\text{S}$ -based SRM was shown [142], the race to demonstrate lower and lower resolutions continued. In this process, samples with gold-coated surfaces, LSP-s with non-equal widths, random geometric patterns with one feature that only in one dimension satisfies the resolution claim and various illumination sources (e.g. coherent, incoherent, filtered, non-filtered) were used. This variety makes it very difficult to compare the results and to determine what is the real limitation of each presented technique. Therefore, standardizing the measurement processes was proposed [143,144]. The key elements of an accurate description would be the following: (i) clear description of *a priori* knowledge, including illumination-type, -wavelength, -filtering and other major components of the optical system (e.g. the type of objective) and post-processing steps; (ii) imaging Siemens star targets or LSP-s with various orientation and equal widths like the USAF 1951 pattern; (iii) considering substrates, such as gold-coated surfaces or fluorescent samples as special cases, and not deducing general conclusions from these measurements. As for wide-field systems, presenting data from different locations within the FoV would be advised. Evaluating new imaging systems based on these principles would benefit the whole community, because it would clarify the exact performances of the proposed methods.

#### 4.4. Dielectric microsphere-based scanning systems

As was mentioned earlier, one realized already in the early works of  $\mu\text{S}$ -based SRM that the FoV is a main limiting factor of these techniques.

It was also shown previously, that this scales with the diameter of the  $\mu\text{S}$ , but the size increment leads to a reduced resolution enhancement. Therefore, other approaches had to be found to overcome this issue. One of the first solutions was presented in 2013 [145]. A micromanipulator was integrated into the imaging system, which could hold and move the  $\mu\text{S}$ -s in any desired position (Fig. 13). This glass rod was mounted on a 3D translational stage and had a movement accuracy of  $\sim 20$  nm. Alternatively, it could be fixed, in which case the sample had to be placed on a motorized microscope stage. The latter solution provided higher accuracy during movements, therefore it was preferred for the imaging experiments. The  $\mu\text{S}$ -s were attached to the glass rod with either air suction or an optical glue. During imaging, the shaft did not influence the super-resolution capabilities of the  $\mu\text{S}$ , because the attachment point was out of the optical path, as was also confirmed by the numerical simulations. The smallest feature (a gap between 500 nm-wide gold structures) detected by the system was  $\sim 73$  nm. This was achieved with silica  $\mu\text{S}$ -s ( $6.1 \pm 0.6$  nm) observed by a  $50\times$ ,  $\text{NA} = 0.55$  objective in air under white light illumination. The positioning technique was found robust, as no sphere was lost or unwillingly deposited during the experiments. This concept was reintroduced two years later [146], when the ethanol-immersed version of it was demonstrated. The added liquid reduced the friction between the glass-probe-actuated  $\mu\text{S}$  and the sample surface. It also acted as a “glue” and ensured good contact between the two objects. Furthermore, a post-processing method was shown, proposing a mosaic-like image stitching to construct a bigger FoV final picture. However, experimentally only a small increment was demonstrated, as the six acquired images of the sample surface,  $2\mu\text{m} \times 2\mu\text{m}$  each, were merged into a final picture showing an area of  $5\mu\text{m} \times 3\mu\text{m}$ . The cause of the shrinkage was in the overlapping, that was used for the stitching.

A novel, extended FoV imaging setup was shown in 2014, when fluorescence correlation microscopy was realized with an array of self-assembled  $\mu\text{S}$ -s [147]. To fabricate such an array, latex  $\mu\text{S}$ -s ( $D = 2\mu\text{m}$ ,  $n_{\text{sphere}} = 1.59$ ) were diluted in water and dispersed on a microscope cover glass. As the water evaporated, the spheres formed a single-layer hexagonal lattice. Then a chamber was formed by covering the chip with another cover glass.  $30\mu\text{m}$  spacers ensured a constant gap between the two of them. Afterwards, the formed chamber was filled with a solution containing fluorescent dyes. The sample was illuminated by a  $\lambda = 633$  nm laser and was observed with a  $10\times$ ,  $\text{NA} = 0.3$  objective. Results showed, that each  $\mu\text{S}$  created a PNJ and each of those could contribute to the global detection volume. This led to an increased detection volume of several tens of femtoliters, while the fluorescent excitation and collection efficiency could be preserved. Furthermore, the diffusion time of a single molecule to cross an analysis spot (i.e. a PNJ) was

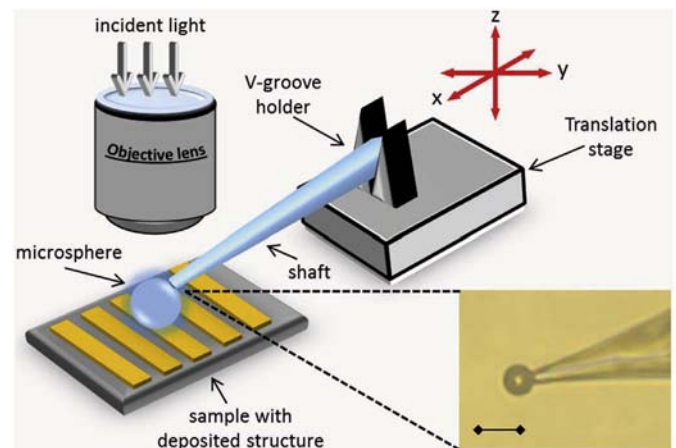


**Fig. 13.** The layout of the optical setup for scanning a  $\mu\text{S}$  over the sample surface with a micropipette. Inset shows a photograph of a  $\mu\text{S}$ , attached to the micropipette. Reprinted by permission from Springer Nature: [145].



reduced, therefore photobleaching could be significantly decreased. Demonstrations showed, that various parameters could be assessed with this technique, including fluorescence brightness, photo-physical blinking, diffusion coefficient and relative hydrodynamic radius. This approach to SRM showed, that imaging with parallel  $\mu$ S-s is possible, if the diameter uniformity is sufficiently high.

These findings were confirmed, when a study showed parallel imaging in wide-field microscopy [138]. The fabrication process described in this work was already shown previously. However, in the last section of the paper, an experiment with multiple  $\mu$ S-s was presented. Uniform BTG  $\mu$ S-s ( $D = 20\mu\text{m}$ ) were closely packed in a  $7.4\mu\text{m}$  thin PDMS film. When an image of the sample was acquired through all of them simultaneously, the generated virtual image was present under all of the  $\mu$ S-s that were placed in the FoV of the microscope objective. It was also shown, that already a couple of  $\mu\text{m}$  difference in the diameter forbids this kind of acquisition, since the FoV of the microscope objective along the z axis is limited. Since the commercially available  $\mu$ S-s typically have bigger deviation than that (e.g. the BTG spheres supplied by Cospheric, CA, USA), the difficulty of large array fabrication was pointed out. Eventually, this set a strict limiting factor on the maximally achievable FoV. As a consequence, research was focused on imaging methods, where the extended FoV is achieved by scanning a  $\mu$ S over the sample.

Chemically powered, autonomous microrobots were introduced to perform such a scanning in 2016 [148]. The concept, called swimming microrobot optical nanoscopy (SMON), utilized high RI  $\mu$ S-s swimming in a media and imaging the sample “on-the-fly”. This could be achieved by selectively coating one side of the  $\mu$ S (polystyrene ( $n_{\text{sphere}} = 1.59$ ) or  $\text{TiO}_2$  ( $n_{\text{sphere}} = 2.1$ ),  $D = 2\text{--}20\mu\text{m}$ ) with a thin Ti/Ni/Pt (2/5/5 nm) layer. This metallic tri-layer served as the “engine” of the microrobot, because it generated a local oxygen gradient through the asymmetric Pt-catalyzed decomposition of the hydrogen peroxide fuel. The fuel was mixed in the aqueous solution that served as the media for imaging. The swimming direction of the  $\mu$ S could be controlled remotely by an external magnet that interacted with the deposited Ni layer. Imaging was demonstrated with various *in silico* samples with feature sizes down to 20 nm. However, all of these patterns had huge pitches (up to  $2\mu\text{m}$ ), from which instead of the resolution limit, only the detection limit of the system could be determined. Another interesting aspect of the work was the image post-processing that allowed to stitch the acquired photographs, therefore map the sample along any desired path. These algorithms also allowed the stitching from parallel sources, enabling scanning with multiple swimming  $\mu$ S-s at the same time. Beside wide-field microscopy, the authors also demonstrated fluorescent imaging of biological samples, however, this was limited due to the toxic nature of the fuel mixed into the immersion medium. The fuel concentration determined the speed of the  $\mu$ S, typically in the range of  $5\text{--}35\mu\text{m/s}$ . The authors envisioned several possible directions of development for SMON, including large area parallel scanning with self-assembled  $\mu$ S-array and real-time, high-resolution imaging of soft biological samples with less toxic fuels such as glucose or urea. Since the trajectory of the scanning is not restricted, computer-controlled scanning along special patterns or features (e.g. tracking of a neuron) also could be realized in the future.

An alternative solution for actuation, presented in the same year, was to combine a dielectric  $\mu$ S with an AFM [149]. Since the AFM instrumentation was a well-proven concept for precise and fine motions, it was a perfect candidate to overcome the FoV limitation of a single  $\mu$ S. The technique was called  $\mu$ S-based scanning superlens microscopy (SSUM) (Fig. 14a). Experimentally, the two components were assembled by fixing a BTG  $\mu$ S to the end of an AFM cantilever with the help of Norland Optical Adhesive (NOA) 63 ultraviolet (UV) curable glue. As it is shown in Fig. 14c–d, the attachment point of the cantilever was on the side of the  $\mu$ S, therefore the optical path was not blocked. The imaging was done purely by an optical microscope, observing the sample through the  $\mu$ S, while the AFM was responsible only for the positioning.

Two operating modes were tested, contact scanning and constant-height scanning, both originating from the AFM instrumentation. In

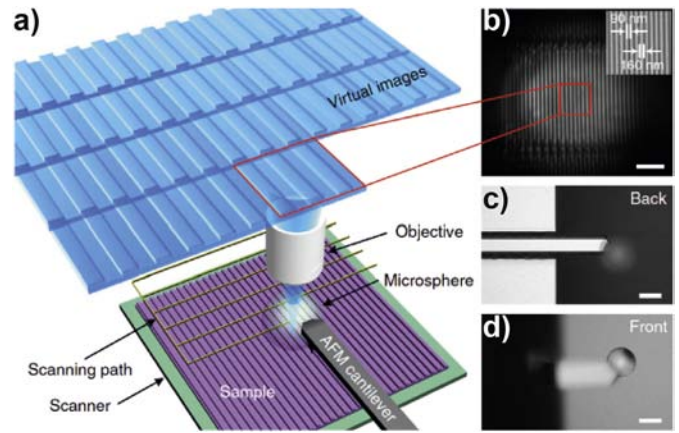


**Fig. 14.** The  $\mu$ S-based SSUM. a) Schematic of the  $\mu$ S-based SSUM, showing the scanning initiated by the AFM instrumentation and the imaging conducted by the dielectric  $\mu$ S. b) Super-resolution virtual image generated by the imaging system as shown in a). Inset shows the SEM image of the sample. Scale bar  $2\mu\text{m}$ . c), d) Photograph of the AFM cantilever attached  $\mu$ S from the back and the front, respectively. Scale bars  $50\mu\text{m}$ . Reprinted from [149] under CC BY 4.0 licence.

the former, the  $\mu$ S was always in direct contact with the sample. To enable this mode, three criteria had to be fulfilled: (i)  $D$  had to be greater than the tip height of the AFM probe, or a probe without a tip had to be used; (ii)  $D$  and the spring constant of the cantilever had to be adjusted to avoid vibrations during scanning, practically,  $D < 80\mu\text{m}$  had to be used; (iii) as mentioned earlier, the attachment point of the cantilever had to be on the side of the  $\mu$ S, in a way that the light path remained clear. Further consideration for  $D$  was to find a balance between the resolution and the FoV. The trade-off here was that the FoV scales with  $D$ , but the smaller  $\mu$ S-s could achieve better resolution. For the demonstration of imaging in this scanning mode, a  $D = 57\mu\text{m}$  BTG  $\mu$ S was used to image LSP-s (Fig. 14b). The smallest pitch shown in this paper was  $250\text{ nm}$ , but individual features down to  $40\text{ nm}$  were also resolved.

In the second scanning mode, the challenge was to establish a height, where the  $\mu$ S was still close enough for capturing the evanescent waves. Both theoretical calculations and experiments showed that this value should be maximum  $\sim 0.65\text{--}0.8\mu\text{m}$  for a  $D = 60\mu\text{m}$   $\mu$ S under white-light illumination. This imaging mode was found to be particularly useful when imaging biological samples (e.g. cells), because they usually have bigger height variance than *in silico* samples and with this scanning mode, damaging of the sample can be avoided. The authors also showed various image processing software packages that could perform the post-processing (i.e. the stitching) of the acquired images. These used automated algorithms to match the individual image tiles, which produced fine results, however, the process could be very time consuming for mapping large areas. Unfortunately, due to the huge variety in experimental parameters through the demonstrated images (e.g. unfiltered halogen light source, various  $\mu$ S diameters, samples containing non-comparable geometrical patterns), it is difficult to determine the exact resolution of the presented system. Although the super-resolution imaging capability was proven, the biggest drawback of this concept is the operation of the AFM instrumentation that is sensitive on vibrations and compared to previously shown methods, complex to handle.

A very similar imaging method was shown in the following year [150]. In that case, the  $\mu$ S was attached to an AFM cantilever with electrostatic forces instead of the optical glue. This could be achieved by fabricating a  $3.5\mu\text{m}$  hole in the cantilever by focused ion beam lithography. This hole allowed the imaging to operate both in transmission and reflectance mode and kept the  $D = 4.6\mu\text{m}$  silica  $\mu$ S fixed. Due to this connection method, it was also possible to release the  $\mu$ S on the sample and picking it up after imaging, however, the authors pointed out that the imaging was not hindered by the presence of the cantilever. They also



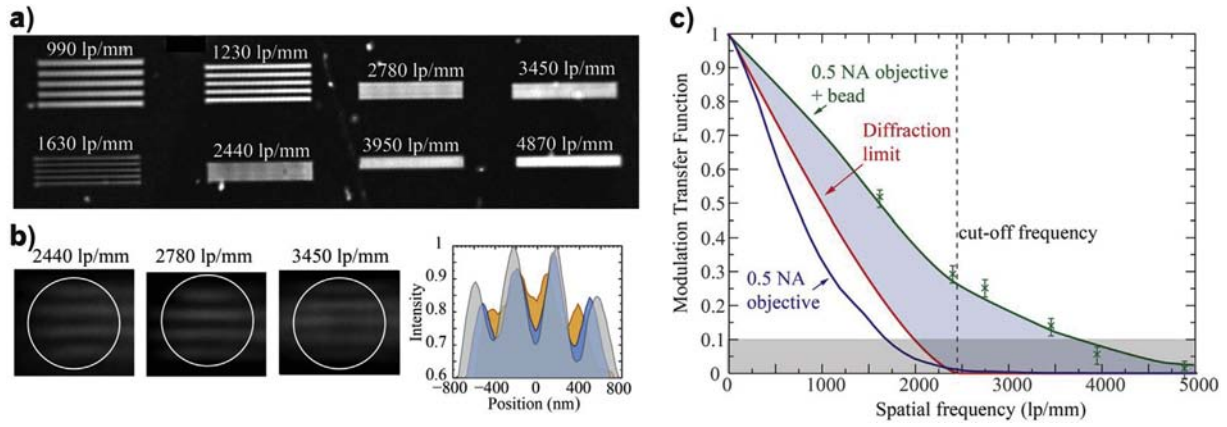


**Fig. 15.** Optical response in  $\mu$ S-based, AFM assisted brightfield microscopy. a) Photograph of LSP-s with various pitches (with their values given as line-pairs/mm), taken with a  $50\times$ ,  $NA = 0.5$  objective without the presence of a  $\mu$ S. b) Details of the same pattern observed through a  $\mu$ S-s with the corresponding intensity profiles along a vertical measurement line (not shown) on the right. c) Frequency response of the imaging system with and without a  $\mu$ S. The blue and the red lines show the measured and the theoretical values produced by the objective alone, respectively. The green line shows the measured values with the  $\mu$ S. The gray area indicates the minimum modulation difference needed for resolving the features according to Rayleigh criteria. The cut-off frequency was calculated based on the Abbe's limit of a system with  $NA = 0.5$ . The highlighted area between the red and the green lines is the resolution gain achieved by the  $\mu$ S. Reprinted from [150] under CC BY 4.0 licence.

emphasized the inconsistency in previously published resolution measurement methods and therefore fabricated equally spaced LSP-s with pitches between 100 and 1000 nm. These patterns were then imaged with and without the presence of the  $\mu$ S-s with  $\lambda = 405$  nm illumination in transmission mode (Fig. 15a–b). Results showed, that  $\mu$ S-assisted imaging could resolve higher spatial frequencies than the  $50\times$ ,  $NA = 0.5$  objective alone. Analysing the intensity values across the LSP-s, allowed the authors to calculate the frequency response (i.e. the modulation transfer function (MTF)) of both systems (Fig. 15c). The calculated data indicated that the  $\mu$ S-assisted system could produce higher modulation for low spatial frequencies and allowed the information transfer of higher ones that otherwise would be lost. A considerable conclusion was given at the end of this work, demonstrating that despite the  $\mu$ S-assisted system could improve the achievable resolution for a low NA imaging system, its absolute performance was not better than the one of the commercially available best NA objective for the given medium.

In parallel, an alternative scanning method was presented in 2017 [151]. Here, a  $\mu$ S ( $D = 40$   $\mu$ m, BTG) was glued to thin glass slide that was kept in constant position relative to the microscope objective via a custom metal frame. Meanwhile, the sample to be imaged was fixed

on a motorized microscope stage that executed a pre-defined scanning and image acquisition. Finally, these pictures were processed and composed into an increased field-of-view, super-resolution image. The performance of this system was analysed by imaging LSP-s with various pitches, but as the halogen light source was not filtered, the precise calculation of the resolution gain is not feasible.

Recently, a new implementation of thin-film-embedded  $\mu$ S-s was shown [152]. To enable scanning, a custom adaptor was designed that synchronized the position of the so-called superlens and the microscope objective. The superlens was fabricated in a previously demonstrated way [138]: BTG  $\mu$ S-s with diameters between 3 and  $80\mu$ m were fixed randomly in a PDMS layer. After curing the PDMS, the superlens was glued to the bottom of the plastic adaptor that was prepared by 3D printing. Due to carefully designed dimensions, the adaptor could be moved along the z axis, therefore it could be positioned in a way that the microscope objective could focus on the virtual image plane generated by the sample upon being observed through the  $\mu$ S-s.

To evaluate the static imaging performance of this system, two samples were imaged. First, the surface of a Blu-ray disc was observed with a  $100\times$ ,  $NA = 0.9$  objective under unfiltered white-light illumination

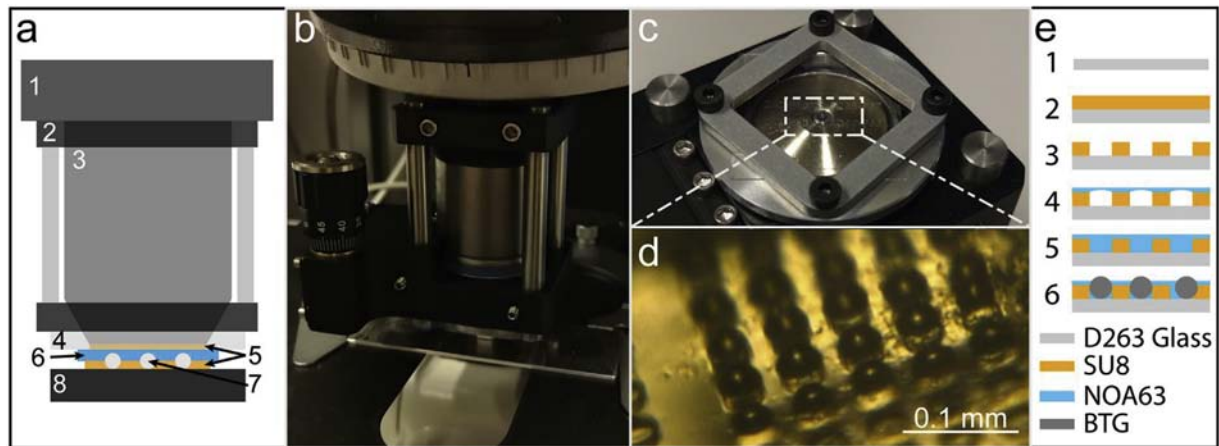


**Fig. 16.** The imaging setup of the scanning microlens array-based optical SRM. a) Schematic of the optical microscope with our imaging setup attached. 1: Microscope revolver. 2: Optical cage (black) with spacers (metallic rods). 3: Microscope objective. 4: Aluminium adapter. 5: Immersion oil. 6: Chip template. 7: BTG  $\mu$ S. 8: Sample to be imaged. b) Photograph of the optical cage system and the Z-axis translator. c) Photograph of the bottom part of the optical cage with a custom aluminium holder attached to the Z-axis translator that clamps a glass  $\mu$ S array chip. d) Photograph of the fabricated  $\mu$ S array chip, showing that the  $\mu$ S-s emerge from the surface plane of the chip. e) Schematic of the fabrication process of the  $\mu$ S array chip. 1: A cover glass chip is treated with oxygen plasma. 2:  $20\mu$ m SU8 photoresist is spin-coated on the chip. 3: An array of microwells is patterned into the SU8 with photolithography. 4: A layer of NOA 63 optical glue is placed on the top, leading to air bubbles stuck into the microwells. 5: The air bubbles are removed with vacuum treatment. 6: BTG  $\mu$ S-s are patterned into the microwells and fixed by UV curing of the optical glue. Reprinted from [153] under CC BY 4.0 licence.

( $400\text{ nm} < \lambda < 700\text{ nm}$ ). Both  $D = 22\mu\text{m}$  and  $D = 67\mu\text{m}$  BTG  $\mu\text{S}$ -s could resolve the features on the surface of the Blu-ray disc. These results did not show much improvement in the achieved resolution, as the pitch of the LSP on the disc surface was  $300\text{ nm}$  while the microscope's Abbe-resolution-limit without the  $\mu\text{S}$ -s was between  $222\text{ nm}$  and  $389\text{ nm}$  depending on the wavelength of the light. The second sample was a cluster of adenoviruses that consisted of  $90\text{--}100\text{ nm}$  individual elements. These were detected by a  $D = 70\mu\text{m}$  sphere, but from this result, the general resolution limit of the imaging system could not be deducted. Demonstrating the scanning mode of the setup was not a straightforward operation, as the PDMS superlens caused such a big friction on the sample that imaging biological objects became impossible. *In silico* structures were possible to image only when a special lubricant (WD40) was applied. Finally, extended FoV images were made, where a custom stitching algorithm was demonstrated. This worked in a sequential way and it calculated the optimal offset between adjacent extracted regions, based on maximizing the normalized cross correlation. Final images were also smoothed by alpha blending. The end results showed good image quality, but the time consumption of this process was not discussed.

One of the newest implementation of  $\mu\text{S}$ -based SRM is the improved version of the previously shown scanning technique, where the glass slide-attached  $\mu\text{S}$  was mechanically fixed to the objective [153]. The basic idea remain unchanged, but multiple  $\mu\text{S}$ -s were employed in parallel and the imaging system was constructed in a more robust way (Fig. 16). A micro-fabricated array of ordered  $\mu\text{S}$ -s was scanned over the sample using a customized algorithm that moved step-by-step a motorized stage, meanwhile the microscope-mounted camera was taking pictures at every step. Then, the extracted central parts of the virtual images that showed super-resolution were stitched together into a mosaic image. The imaging system was analysed based on its lateral resolution and FoV. The former was measured to be  $240\text{ nm}$  with  $\lambda = 545 \pm 20\text{ nm}$  and an oil-immersion,  $NA = 1.4$  objective. Although that was not a huge resolution gain ( $\sim 15\%$ , based on the measurements presented in the paper), the demonstrated FoV was very impressive, as  $0.5 \times 1.0$  surface area was imaged. The main advantages of this technique compared to the AFM-based ones are the more robust and cost-effective instrumentation and the faster algorithmic post-processing.

As conclusion for the presented  $\mu\text{S}$ -based SRM techniques, the advantages of these systems in terms of cost-effectiveness to more complex super-resolution methods are evident. The possible application range for these kind of microscopy methods extends through the fields of *in vitro* metrology, *in vivo* imaging, environmental monitoring, robotics and many other research fields where optical observation of sub-diffraction features is required. However, because of the variety of measurement methods and arbitrary definitions used in the publications, comparison of the achieved resolutions is not straightforward. Furthermore, the extension of the FoV is still an unresolved issue, as pioneering works only started to appear recently. These unsolved issues prohibited the maturing of  $\mu\text{S}$ -based microscopy techniques and their commercialization up until now.

## 5. Discussion

As was pointed out in this review, comparing optical super-resolution techniques can be difficult due to the non-standardized data provided by the authors. Despite of this, in order to provide a general overview, the currently available optical super-resolution methods are evaluated along four important parameters (Fig. 17). Due to the huge amount of techniques, the methods were grouped based on their imaging principle and plotted on two spider-diagrams. These were constructed in a way that a microscopy technique can reach three levels along the four axes. If a microscope can provide very low resolution, high FoV, quick imaging and is cost-effective, then it would reach the maximum diameter circle along all of these axes. Wide-field microscopy was chosen as reference in both representations of Fig. 17. The upper

diagram shows the four main groups of far-field super-resolution microscopies: (i) confocal techniques like the 4Pi microscopy (blue); (ii) PSF-shaping techniques like the STED (green); (iii) Moiré-effect-based structured illumination microscopies (red); and (iv) single molecule localization microscopy techniques (yellow). It is clearly visible in this representation, that these methods are optimized for maximum lateral resolution, while the cost of the imaging system and the imaging time were not primary design aspects. In the case of the confocal techniques, the imaging time and the cost of the instrumentation increased, while the FoV remained similar to the wide-field microscopy. Other far-field techniques sacrificed even the FoV to further increase the resolution. However, a common drawback for these techniques is that only fluorescent samples can be imaged. To avoid these inconveniences, one can choose to use one of the techniques presented on the lower diagram

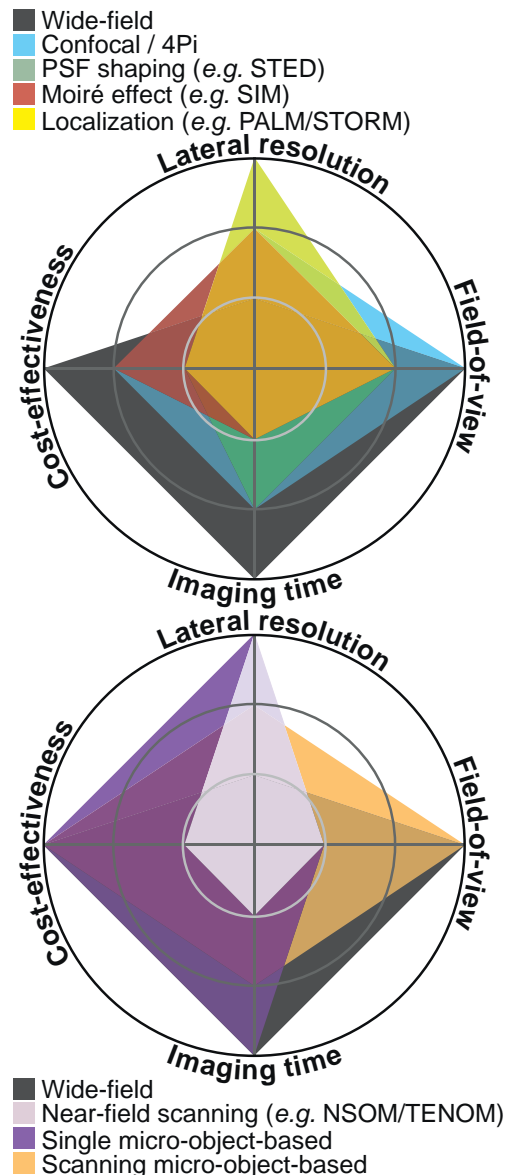


Fig. 17. Comparison of optical super-resolution microscopies in terms of lateral resolution, field-of-view, imaging time and cost effectiveness.

of Fig. 17. Here, the performance of the near-field techniques (prim), the single, non-scanning micro-object-based techniques (purple) and the scanning micro-object-based techniques (gold) are shown along the same evaluation criteria. The advantage of the single micro-object-based microscopies is evident, as they can outperform the near-field techniques in terms of cost and imaging time, while they do not provide significantly lower resolution. However, both techniques suffer from the restricted FoV and working distance. Furthermore, they are only able to image the surface of the sample, due to theoretical restrictions. In the case of the scanning versions of the micro-object-based imaging, larger diameter  $\mu$ S-s are employed, which results in a degraded resolution. Furthermore, the scanning procedure can be time-consuming, therefore, this group's performance along that axis is also weaker. Comparing the scanning micro-object-based techniques with the far-field microscopies shows that the performance of the former is comparable with the confocal techniques, but that they have a significant price advantage. Finally, it is important to note that this comparison is not complete, as parameters like bio-compatibility, restricted specimens (e.g. fluorescent dyes needed for imaging), sample preparation time, artefacts, axial resolution or imaging depth were not taken into account. Considering all these parameters would increase the complexity of the analysis, which would considerably be beyond the scope of this review, as the main goal of the current work is to demonstrate the new, emerging branch of optical super-resolution microscopy, that is potent and competitive against the “old” contenders. We envision that the huge effort from the scientific community that is invested today into the development of these micro-object-based imaging techniques will result in even better performing and more versatile microscopy methods in the near future.

### Conflict of Interest Statement

The authors declare that they have no competing interests.

### Acronyms

$\mu$ S	microsphere
2D	two-dimensional
3D	three-dimensional
AFM	atomic force microscopy
BALM	binding-activated localization microscopy
BTG	barium titanate glass
CCD	charge-coupled device
CFM	confocal fluorescence microscopy
CO <sub>2</sub>	carbon dioxide
COLD	cryogenic optical localization in 3D
DNA	deoxyribonucleic acid
DSTORM	direct STORM
FDTD	finite-difference time-domain
FPS	frames per second
FWHM	full width at half-maximum
FoV	field-of-view
GSDIM	ground state depletion microscopy followed by individual molecule return
GSD	ground-state-depletion
HF	hydrofluoric acid
IPA	isopropyl alcohol
laser	light amplification by stimulated emission of radiation
LED	light emitting diode
LSP	lines-and-spaces pattern
MTF	modulation transfer function
NA	numerical aperture
NOA	Norland Optical Adhesive
NORM	near-field optical random mapping
NSOM	near-field scanning optical microscopy
ON	(white-light) optical nanoscopy

PALM/FPALM	photoactivated localization microscopy/fluorescence photoactivation localization microscopy
PALMIRA	PALM with independently running acquisition
PDMS	poly(dimethylsiloxane)
PNJ	photonic nanojet
PSF	point spread function
PSTM	photon scanning tunneling microscopy
PTM	photon tunneling microscopy
RI	refractive index
RPM	reversible photo-bleaching microscopy
SEM	scanning electron microscopy
SIL	solid immersion lens
SIM	structured illumination microscopy
SMI	spatially modulated illumination
SMLM	single molecule localization microscopy
SMON	swimming microrobot optical nanoscopy
SNR	signal-to-noise ratio
SOFI	super-resolution optical fluctuation imaging
SPDM	spectral precision distance/spectral position determination microscopy
SRM	super-resolution microscopy
SSIM	saturated structured illumination microscopy
SSUM	scanning superlens microscopy
STED	stimulated-emission-depletion
STM	scanning tunneling microscopy
STOM	scanning tunneling optical microscopy
STORM	stochastic optical reconstruction microscopy
SiO <sub>2</sub>	silicon dioxide
TENOM	tip-enhanced near-field optical microscopy
TiO <sub>2</sub>	titanium dioxide
UV	ultraviolet

### Symbols

D ( $\mu$ m)	diameter of the focusing curvature of the microobject/diameter of the microsphere
d (nm)	diffraction limit
I (W/m <sup>2</sup> )	intensity of the light
$n_{\text{medium}}$	refractive index of the medium
$n_{\text{sphere}}$	refractive index of the microsphere
$\lambda$ (nm)	wavelength of the light

### Acknowledgements

The authors would like to thank for Swiss National Science Foundation Grant (200021-152948) for funding this project.

### References

- [1] S.W. Hell, Far-field optical nanoscopy, *Science* 316 (5828) (2007) 1153–1158, <https://doi.org/10.1126/science.1137395>.
- [2] B. Huang, M. Bates, X. Zhuang, Super-resolution fluorescence microscopy, *Annu. Rev. Biochem.* 78 (1) (2009) 993–1016, <https://doi.org/10.1146/annurev.biochem.77.061906.092014>.
- [3] L. Schermelleh, R. Heintzmann, H. Leonhardt, A guide to super-resolution fluorescence microscopy, *J. Cell Biol.* 190 (2) (2010) 165–175, <https://doi.org/10.1083/jcb.201002018>.
- [4] B.O. Leung, K.C. Chou, Review of super-resolution fluorescence microscopy for biology, *Appl. Spectrosc.* 65 (9) (2011) 967–980, <https://doi.org/10.1366/11-06398>.
- [5] B. Hecht, B. Sick, U.P. Wild, V. Deckert, R. Zenobi, O.J. Martin, D.W. Pohl, Scanning near-field optical microscopy with aperture probes: Fundamentals and applications, *J. Chem. Phys.* 112 (18) (2000) 7761–7774, <http://scitation.aip.org/content/aip/journal/jcp/112/18/10.1063/1.481382>.
- [6] N. Mauser, A. Hartschuh, Tip-enhanced near-field optical microscopy, *Chem. Soc. Rev.* 43 (4) (2014) 1248–1262, <https://doi.org/10.1039/C3CS60258C>.
- [7] H. Yang, M.A.M. Gijs, Micro-optics for microfluidic analytical applications, *Chem. Soc. Rev.* 47 (4) (2018) 1391–1458, <https://doi.org/10.1039/C5CS00649J>.
- [8] B.S. Luk'yanchuk, R. Paniagua-Domínguez, I. Minin, O. Minin, Z. Wang, Refractive index less than two: photonic nanojets yesterday, today and tomorrow [Invited], *Optical Mater. Express* 7 (6) (2017) 1820, <https://doi.org/10.1364/OME.7.001820>.



- [9] S.D. Hell, Double-confocal scanning microscope, *cIB: G02B21/00*; (IPC1-7): G02B21/00, Jun. 1992, [https://worldwide.espacenet.com/publicationDetails/biblio?FT=D&date=19920624&DB=EPODOC&locale=en\\_EP&CC=EP&NR=0491289A1&KC=A1&ND=4](https://worldwide.espacenet.com/publicationDetails/biblio?FT=D&date=19920624&DB=EPODOC&locale=en_EP&CC=EP&NR=0491289A1&KC=A1&ND=4).
- [10] S. Hell, E. Stelzer, Properties of a 4pi confocal fluorescence microscope, *JOSA A* 9 (12) (1992) 2159–2166.
- [11] S. Hell, E.H.K. Stelzer, Fundamental improvement of resolution with a 4pi-confocal fluorescence microscope using two-photon excitation, *Opt. Commun.* 93 (5–6) (1992) 277–282.
- [12] S.W. Hell, S. Lindek, C. Cremer, E.H. Stelzer, Confocal microscopy with an increased detection aperture: type-B 4pi confocal microscopy, *Opt. Lett.* 19 (3) (1994) 222–224.
- [13] S.W. Hell, Improvement of lateral resolution in far-field fluorescence light microscopy by using two-photon excitation with offset beams, *Opt. Commun.* 106 (1–3) (1994) 19–24.
- [14] S.W. Hell, J. Wichmann, Breaking the diffraction resolution limit by stimulated emission: stimulated-emission-depletion fluorescence microscopy, *Opt. Lett.* 19 (11) (1994) 780–782.
- [15] S.W. Hell, M. Kroug, Ground-state-depletion fluorescence microscopy: A concept for breaking the diffraction resolution limit, *Appl. Phys. B* 60 (5) (1995) 495–497.
- [16] S. Bretschneider, C. Eggeling, S.W. Hell, Breaking the diffraction barrier in fluorescence microscopy by optical shelving, *Phys. Rev. Lett.* 98 (21) (2007), <https://doi.org/10.1103/PhysRevLett.98.218103>.
- [17] The Nobel Prize in Chemistry 2014 - Prize Announcement, [https://www.nobelprize.org/nobel\\_prizes/chemistry/laureates/2014/announcement.html](https://www.nobelprize.org/nobel_prizes/chemistry/laureates/2014/announcement.html).
- [18] M.G. Gustafsson, Surpassing the lateral resolution limit by a factor of two using structured illumination microscopy, *J. Microsc.* 198 (2) (2000) 82–87, <http://onlinelibrary.wiley.com/doi/10.1046/j.1365-2818.2000.00710.x/full>.
- [19] E. Rittweger, D. Wildanger, S.W. Hell, Far-field fluorescence nanoscopy of diamond color centers by ground state depletion, *EPL (Europhys. Lett.)* 86 (1) (2009), 14001, <https://doi.org/10.1209/0295-5075/86/14001>.
- [20] M.G. Gustafsson, Method and Apparatus for Three-Dimensional Microscopy With Enhanced Depth Resolution, <https://patents.google.com/patent/US5671085A/en> Feb. 1995.
- [21] M.G.L. Gustafsson, Nonlinear structured-illumination microscopy: wide-field fluorescence imaging with theoretically unlimited resolution, *Proc. Natl. Acad. Sci. U. S. A.* 102 (37) (2005) 13081–13086.
- [22] M. Hausmann, B. Schneider, J. Bradl, C.G. Cremer, High-precision distance microscopy of 3d nanostructures by a spatially modulated excitation fluorescence microscope, *Optical Biopsies and Microscopic Techniques II*, Vol. 3197, International Society for Optics and Photonics 1997, pp. 217–223.
- [23] B. Schneider, J. Bradl, I. Kirsten, M. Hausmann, C. Cremer, High Precision Localization of Fluorescent Targets in the Nanometer Range by Spatially Modulated Excitation Fluorescence Microscopy, *Fluorescence Microscopy and Fluorescent Probes*, Vol. 2, 1998 63–68.
- [24] B. Schneider, I. Uppmann, I. Kirsten, J. Bradl, M. Hausmann, C. Cremer, A dual-laser, spatially modulated illumination fluorescence microscope, *Microsc. Anal.* (1999) 5–8.
- [25] B. Albrecht, A.V. Failla, A. Schweitzer, C. Cremer, Spatially modulated illumination microscopy allows axial distance resolution in the nanometer range, *Appl. Opt.* 41 (1) (2002) 80–87.
- [26] H. Bornfleth, K. Sätzler, R. Eils, C. Cremer, High-precision distance measurements and volume-conserving segmentation of objects near and below the resolution limit in three-dimensional confocal fluorescence microscopy, *J. Microsc.* 189 (2) (1997) 118–136.
- [27] C. Cremer, M. Hausmann, J. Bradl, B. Rinke, Method and Devices for Measuring Distances Between Object Structures, <https://patents.google.com/patent/US6424421/en> Jul. 2002.
- [28] A.M. Van Oijen, J. Köhler, J. Schmidt, M. Müller, G.J. Brakenhoff, 3-Dimensional super-resolution by spectrally selective imaging, *Chem. Phys. Lett.* 292 (1–2) (1998) 183–187.
- [29] K.A. Lidke, B. Rieger, T.M. Jovin, R. Heintzmann, Superresolution by localization of quantum dots using blinking statistics, *Opt. Express* 13 (18) (2005) 7052–7062.
- [30] S.T. Hess, T.P. Girirajan, M.D. Mason, Ultra-high resolution imaging by fluorescence photoactivation localization microscopy, *Biophys. J.* 91 (11) (2006) 4258–4272, <https://doi.org/10.1529/biophysj.106.091116>.
- [31] E. Betzig, G.H. Patterson, R. Sougrat, Imaging intracellular fluorescent proteins at nanometer resolution, *Science* 313 (5793) (2006) 1642–1645, <https://doi.org/10.1126/science.1130258>.
- [32] S.T. Hess, T.J. Gould, M.V. Gudheti, S.A. Maas, K.D. Mills, J. Zimmerberg, Dynamic clustered distribution of hemagglutinin resolved at 40 nm in living cell membranes discriminates between raft theories, *Proc. Natl. Acad. Sci.* 104 (44) (2007) 17370–17375.
- [33] C. Geisler, A. Schönl, C. von Middendorff, H. Bock, C. Eggeling, A. Egner, S. Hell, Resolution of  $\lambda/10$  in fluorescence microscopy using fast single molecule photo-switching, *Appl. Phys. A* 88 (2) (2007) 223–226, <https://doi.org/10.1007/s00339-007-4144-0>.
- [34] M.J. Rust, M. Bates, X. Zhuang, Sub-diffraction-limit imaging by stochastic optical reconstruction microscopy (STORM), *Nat. Methods* 3 (10) (2006) 793–796, <https://doi.org/10.1038/nmeth929>.
- [35] M. Bates, T.R. Blosser, X. Zhuang, Short-range spectroscopic ruler based on a single-molecule optical switch, *Phys. Rev. Lett.* 94 (10) (2018), <https://doi.org/10.1103/PhysRevLett.94.108101>.
- [36] M. Heilemann, S. van de Linde, M. Schüttelz, R. Kasper, B. Seefeldt, A. Mukherjee, P. Tinnefeld, M. Sauer, Subdiffraction-resolution fluorescence imaging with conventional fluorescent probes, *Angew. Chem. Int. Ed.* 47 (33) (2008) 6172–6176, <https://doi.org/10.1002/anie.200802376>.
- [37] J. Fölling, M. Bossi, H. Bock, R. Medda, C.A. Wurm, B. Hein, S. Jakobs, C. Eggeling, S.W. Hell, Fluorescence nanoscopy by ground-state depletion and single-molecule return, *Nat. Methods* 5 (11) (2008) 943–945, <https://doi.org/10.1038/nmeth.1257>.
- [38] D. Baddeley, I.D. Jayasinghe, C. Cremer, M.B. Cannell, C. Soeller, Light-induced dark states of organic fluochromes enable 30 nm resolution imaging in standard media, *Biophys. J.* 96 (2) (2009) L22–L24, <https://doi.org/10.1016/j.bpj.2008.11.002>.
- [39] T. Dertinger, R. Colyer, G. Iyer, S. Weiss, J. Enderlein, Fast, background-free, 3d super-resolution optical fluctuation imaging (SOFI), *Proc. Natl. Acad. Sci.* 106 (52) (2009) 22287–22292.
- [40] T. Dertinger, R. Colyer, R. Vogel, J. Enderlein, S. Weiss, Achieving increased resolution and more pixels with Superresolution Optical Fluctuation Imaging (SOFI), *Opt. Express* 18 (18) (2010) 18875–18885.
- [41] R. Kaufmann, P. Müller, M. Hausmann, C. Cremer, Imaging label-free intracellular structures by localisation microscopy, *Micron* 42 (4) (2011) 348–352, <https://doi.org/10.1016/j.micron.2010.03.006>.
- [42] I. Schoen, J. Ries, E. Klotzsch, H. Ewers, V. Vogel, Binding-activated localization microscopy of DNA structures, *Nano Lett.* 11 (9) (2011) 4008–4011, <https://doi.org/10.1021/nl2025954>.
- [43] S. Weisenburger, D. Boening, B. Schomburg, K. Giller, S. Becker, C. Griesinger, V. Sandoghdar, Cryogenic optical localization provides 3d protein structure data with Angstrom resolution, *Nat. Methods* 14 (2) (2017) 141–144, <https://doi.org/10.1038/nmeth.4141>.
- [44] J.W. Goodman, *Introduction to Fourier Optics*, Roberts and Company Publishers, 2005.
- [45] G. Binnig, H. Rohrer, Scanning tunneling microscopy, *Surf. Sci.* 126 (1983) 236–244.
- [46] G. Binnig, C.F. Quate, Atomic force microscope, *Phys. Rev. Lett.* 56 (9) (1986) 5.
- [47] J.M. Guerra, Photon tunneling microscopy, *Appl. Opt.* 29 (26) (1990) 3741–3752.
- [48] E.H. Syngé, A suggested method for extending microscopic resolution into the ultra-microscopic region, *Lond. Edinb. Dublin Philos. Mag. J. Sci.* 6 (35) (1928) 356–362, <https://doi.org/10.1080/14786440808564615>.
- [49] D.W. Pohl, W. Denk, M. Lanz, Optical stethoscopy: image recording with resolution  $\lambda/20$ , *Appl. Phys. Lett.* 44 (7) (1984) 651–653, <https://doi.org/10.1063/1.94865>.
- [50] A. Lewis, M. Isaacson, A. Harootunian, A. Muray, Development of a 500 Å spatial resolution light microscope: I. light is efficiently transmitted through  $\lambda/16$  diameter apertures, *Ultramicroscopy* 13 (3) (1984) 227–231, [https://doi.org/10.1016/0304-3991\(84\)90201-8](https://doi.org/10.1016/0304-3991(84)90201-8).
- [51] A. Harootunian, E. Betzig, M. Isaacson, A. Lewis, Super-resolution fluorescence near-field scanning optical microscopy, *Appl. Phys. Lett.* 49 (11) (1986) 674–676, <https://doi.org/10.1063/1.97565>.
- [52] U. Dürig, D.W. Pohl, F. Rohner, Near-field optical-scanning microscopy, *J. Appl. Phys.* 59 (10) (1986) 3318–3327, <https://doi.org/10.1063/1.336848>.
- [53] E. Betzig, M. Isaacson, A. Lewis, Collection mode near-field scanning optical microscopy, *Appl. Phys. Lett.* 51 (25) (1987) 2088–2090, <https://doi.org/10.1063/1.98956>.
- [54] H. Heinzelmann, B. Hecht, L. Novotny, D.W. Pohl, Forbidden light scanning near-field optical microscopy, *J. Microsc.* 177 (2) (1995) 115–118, <https://doi.org/10.1111/j.1365-2818.1995.tb03541.x>.
- [55] B. Hecht, H. Heinzelmann, D.W. Pohl, Combined aperture SNOM/PSTM: best of both worlds? *Ultramicroscopy* 57 (2) (1995) 228–234, [https://doi.org/10.1016/0304-3991\(94\)00144-C](https://doi.org/10.1016/0304-3991(94)00144-C).
- [56] U.C. Fischer, D.W. Pohl, Observation of single-particle plasmons by near-field optical microscopy, *Phys. Rev. Lett.* 62 (4) (1989) 458–461, <https://doi.org/10.1103/PhysRevLett.62.458>.
- [57] F. Zenhausern, Y. Martin, H.K. Wickramasinghe, Scanning interferometric apertureless microscopy: optical imaging at 10 angstrom resolution, *Science* 269 (5227) (1995) 1083–1085, <https://doi.org/10.1126/science.269.5227.1083>.
- [58] Y. Inoué, S. Kawata, A scanning near-field optical microscope having scanning electron tunnelling microscope capability using a single metallic probe tip, *J. Microsc.* 178 (1) (1995) 14–19, <https://doi.org/10.1111/j.1365-2818.1995.tb03575.x>.
- [59] P. Gleyzes, A.C. Boccara, R. Bachelot, Near field optical microscopy using a metallic vibrating tip, *Ultramicroscopy* 57 (2) (1995) 318–322, [https://doi.org/10.1016/0304-3991\(94\)00160-0](https://doi.org/10.1016/0304-3991(94)00160-0).
- [60] C. Girard, O.J.F. Martin, A. Dereux, Molecular lifetime changes induced by nanometer scale optical fields, *Phys. Rev. Lett.* 75 (17) (1995) 3098–3101, <https://doi.org/10.1103/PhysRevLett.75.3098>.
- [61] J. Koglin, U. Fischer, H. Fuchs, Scanning near-field optical microscopy with a tetrahedral tip at a resolution of 6 nm, *J. Biomed. Opt.* 1 (1) (1996) 75–79, <https://doi.org/10.1117/12.227700>.
- [62] Sugiura, Kawata, Okada, Fluorescence imaging with a laser trapping scanning near-field optical microscope, *J. Microsc.* 194 (2–3) (1999) 291–294, <https://doi.org/10.1046/j.1365-2818.1999.00523.x>.
- [63] B. Knoll, F. Keilmann, Near-field probing of vibrational absorption for chemical microscopy, *Nature* 399 (6732) (1999) 134–137, <https://doi.org/10.1038/20154>.
- [64] D. Courjon, Scanning Tunneling Optical Microscopy, *Scanning Tunneling Microscopy and Related Methods*, NATO ASI Series, Springer, Dordrecht 1990, pp. 497–505, [https://doi.org/10.1007/978-94-015-7871-4\\_28](https://doi.org/10.1007/978-94-015-7871-4_28).
- [65] R.C. Reddick, R.J. Warmack, T.L. Ferrell, New form of scanning optical microscopy, *Phys. Rev. B* 39 (1) (1989) 767–770, <https://doi.org/10.1103/PhysRevB.39.767>.



- [66] E. Betzig, J.K. Trautman, T.D. Harris, J.S. Weiner, R.L. Kostelak, Breaking the diffraction barrier: optical microscopy on a nanometric scale, *Science* 251 (5000) (1991) 1468–1470, <https://doi.org/10.1126/science.251.5000.1468>.
- [67] G.A. Valaskovic, M. Holton, G.H. Morrison, Parameter control, characterization, and optimization in the fabrication of optical fiber near-field probes, *Appl. Opt.* 34 (7) (1995) 1215–1228, <https://doi.org/10.1364/AO.34.001215>.
- [68] D.R. Turner, Etch Procedure for Optical Fibers, <https://patents.google.com/patent/US4469554A/en> Sep. 1984.
- [69] P. Hoffmann, B. Dutoit, R.-P. Salathé, Comparison of mechanically drawn and protection layer chemically etched optical fiber tips, *Ultramicroscopy* 61 (1) (1995) 165–170, [https://doi.org/10.1016/0304-3991\(95\)00122-0](https://doi.org/10.1016/0304-3991(95)00122-0).
- [70] P. Lambelet, A. Sayah, M. Pfeffer, C. Philippon, F. Marquis-Weible, Chemically etched fiber tips for near-field optical microscopy: a process for smoother tips, *Appl. Opt.* 37 (31) (1998) 7289–7292, <https://doi.org/10.1364/AO.37.007289>.
- [71] H.A. Bethe, Theory of diffraction by small holes, *Phys. Rev.* 66 (7–8) (1944) 163–182, <https://doi.org/10.1103/PhysRev.66.163>.
- [72] C.J. Bouwkamp, On Bethe's theory of diffraction by small holes, *Philips Res. Rep.* 5 (1950) 321–332.
- [73] J.-J. Greffet, R. Carminati, Image formation in near-field optics, *Prog. Surf. Sci.* 56 (3) (1997) 133–237, [https://doi.org/10.1016/S0079-6816\(98\)00004-5](https://doi.org/10.1016/S0079-6816(98)00004-5).
- [74] O.J.F. Martin, N.B. Piller, Electromagnetic scattering in polarizable backgrounds, *Phys. Rev. E* 58 (3) (1998) 3909–3915, <https://doi.org/10.1103/PhysRevE.58.3909>.
- [75] C. Girard, A. Dereux, Near-field optics theories, *Rep. Prog. Phys.* 59 (5) (1996) 657, <https://doi.org/10.1088/0034-4885/59/5/002>.
- [76] S. Jutamulia, M. Ohtsu, T. Asakura, Near-Field Optics: Physics, Devices, and Information Processing, Vol. 3791, 1999 <http://adsabs.harvard.edu/abs/1999SPIE.3791.....J>.
- [77] Martin, 3d simulations of the experimental signal measured in near-field optical microscopy, *J. Microsc.* 194 (2–3) (1999) 235–239, <https://doi.org/10.1046/j.1365-2818.1999.00560.x>.
- [78] A. Lewis, H. Taha, A. Strinkovski, A. Manevitch, A. Khachatourians, R. Dekhter, E. Ammann, Near-field optics: from subwavelength illumination to nanometric shadowing, *Nat. Biotechnol.* 21 (11) (2003) 1378–1386, <https://doi.org/10.1038/nbt898>.
- [79] J. Wessel, Surface-enhanced optical microscopy, *JOSA B* 2 (9) (1985) 1538–1541, <https://doi.org/10.1364/JOSA.2.001538>.
- [80] R. Hillenbrand, T. Taubner, F. Keilmann, Phonon-enhanced light–matter interaction at the nanometre scale, *Nature* 418 (6894) (2002) 159–162, <https://doi.org/10.1038/nature00899>.
- [81] F. Keilmann, R. Hillenbrand, Near-field microscopy by elastic light scattering from a tip, *Philos. Trans. Royal Soc. Lond. A* 362 (1817) (2004) 787–805, <https://doi.org/10.1098/rsta.2003.1347>.
- [82] A.V. Zayats, V. Sandoghdar, Apertureless scanning near-field second-harmonic microscopy, *Opt. Commun.* 178 (1) (2000) 245–249, [https://doi.org/10.1016/S0030-4018\(00\)00655-6](https://doi.org/10.1016/S0030-4018(00)00655-6).
- [83] A.V. Zayats, I.I. Smolyaninov, Near-field second-harmonic generation, *Philos. Trans. Royal Soc. Lond. A* 362 (1817) (2004) 843–860, <https://doi.org/10.1098/rsta.2003.1350>.
- [84] A. Bouhelier, M. Beversluis, A. Hartschuh, L. Novotny, Near-field second-harmonic generation induced by local field enhancement, *Phys. Rev. Lett.* 90 (1) (2003), 013903, <https://doi.org/10.1103/PhysRevLett.90.013903>.
- [85] M. Danckwerts, L. Novotny, Optical frequency mixing at coupled gold nanoparticles, *Phys. Rev. Lett.* 98 (2) (2007), 026104, <https://doi.org/10.1103/PhysRevLett.98.026104>.
- [86] R.M. Stöckle, Y.D. Suh, V. Deckert, R. Zenobi, Nanoscale chemical analysis by tip-enhanced Raman spectroscopy, *Chem. Phys. Lett.* 318 (1) (2000) 131–136, [https://doi.org/10.1016/S0009-2614\(99\)01451-7](https://doi.org/10.1016/S0009-2614(99)01451-7).
- [87] N. Hayazawa, Y. Inouye, S. Sekkat, S. Kawata, Near-field Raman scattering enhanced by a metallized tip, *Chem. Phys. Lett.* 335 (5) (2001) 369–374, [https://doi.org/10.1016/S0009-2614\(01\)00065-3](https://doi.org/10.1016/S0009-2614(01)00065-3).
- [88] A. Hartschuh, E.J. Sánchez, X.S. Xie, L. Novotny, High-resolution near-field Raman microscopy of single-walled carbon nanotubes, *Phys. Rev. Lett.* 90 (9) (2003), 095503, <https://doi.org/10.1103/PhysRevLett.90.095503>.
- [89] L. Novotny, R.X. Bian, X.S. Xie, Theory of nanometric optical tweezers, *Phys. Rev. Lett.* 79 (4) (1997) 645–648, <https://doi.org/10.1103/PhysRevLett.79.645>.
- [90] M.I. Stockman, S.V. Faleev, D.J. Bergman, Coherent control of femtosecond energy localization in nanosystems, *Phys. Rev. Lett.* 88 (6) (2002), 067402, <https://doi.org/10.1103/PhysRevLett.88.067402>.
- [91] T. Brixner, F.J. García De Abajo, J. Schneider, W. Pfeiffer, Nanoscopic ultrafast space-time-resolved spectroscopy, *Phys. Rev. Lett.* 95 (9) (2005), 093901, <https://doi.org/10.1103/PhysRevLett.95.093901>.
- [92] M.I. Stockman, M.F. Kling, U. Kleineberg, F. Krausz, Attosecond nanoplasmonic-field microscope, *Nat. Photonics* 1 (9) (2007) 539–544, <https://doi.org/10.1038/nphoton.2007.169>.
- [93] M. Aeschlimann, M. Bauer, D. Bayer, T. Brixner, F.J. García De Abajo, W. Pfeiffer, M. Rohrer, C. Spindler, F. Steeb, Adaptive subwavelength control of nano-optical fields, *Nature* 446 (7133) (2007) 301–304, <https://doi.org/10.1038/nature05595>.
- [94] E.M. Purcell, Spontaneous emission probabilities at radio frequencies, *Confined Electrons and Photons*, NATO ASI Series, Springer, Boston, MA, 1995 [https://doi.org/10.1007/978-1-4615-1963-8\\_40](https://doi.org/10.1007/978-1-4615-1963-8_40), 839–839.
- [95] M. Thomas, J.-J. Greffet, R. Carminati, J.R. Arias-Gonzalez, Single-molecule spontaneous emission close to absorbing nanostructures, *Appl. Phys. Lett.* 85 (17) (2004) 3863–3865, <https://doi.org/10.1063/1.1812592>.
- [96] A. Hartschuh, H. Qian, A.J. Meixner, L. Novotny, Nanoscale optical imaging of excitons in single-walled carbon nanotubes, *Nano Lett.* 5 (11) (2005) 2310–2313, <https://doi.org/10.1021/nl051775e>.
- [97] K. Aslan, I. Gryczynski, J. Malicka, E. Matveeva, J.R. Lakowicz, C.D. Geddes, Metal-enhanced fluorescence: an emerging tool in biotechnology, *Curr. Opin. Biotechnol.* 16 (1) (2005) 55–62, <https://doi.org/10.1016/j.copbio.2005.01.001>.
- [98] A. Hartschuh, Tip-enhanced near-field optical microscopy, *Angew. Chem. Int. Ed.* 47 (43) (2008) 8178–8191, <https://doi.org/10.1002/anie.200801605>.
- [99] O. Motoichi, Progress of high-resolution photon scanning tunneling microscopy due to a nanometric fiber probe, *J. Lightwave Technol.* 13 (7) (1995) 1200–1221.
- [100] Y.V. Miklyaev, S.A. Asselborn, K.A. Zaytsev, M.Y. Darscht, Superresolution microscopy in far-field by near-field optical random mapping nanoscopy, *Appl. Phys. Lett.* 105 (11) (2014), 113103, <https://doi.org/10.1063/1.4895922>.
- [101] Z. Chen, A. Taflove, V. Backman, Photonic nanojet enhancement of backscattering of light by nanoparticles: a potential novel visible-light ultramicroscopy technique, *Opt. Express* 12 (7) (2004) 1214–1220.
- [102] S.M. Mansfield, G.S. Kino, Solid immersion microscope, *Appl. Phys. Lett.* 57 (24) (1990) 2615, <https://doi.org/10.1063/1.103828>.
- [103] J.B. Pendry, Negative refraction makes a perfect lens, *Phys. Rev. Lett.* 85 (18) (2000) 3966.
- [104] H. Yang, R. Trouillon, G. Huszka, M.A.M. Gijs, Super-resolution imaging of a dielectric microsphere is governed by the waist of its photonic nanojet, *Nano Lett.* (2016) 4862–4870, <https://doi.org/10.1021/acs.nanolett.6b01255>.
- [105] X. Li, Z. Chen, A. Taflove, V. Backman, Optical analysis of nanoparticles via enhanced backscattering facilitated by 3-D photonic nanojets, *Opt. Express* 13 (2) (2005) 526–533 <http://www.opticsinfobase.org/abstract.cfm?uri=OE-13-2-526>.
- [106] S. Lecler, Y. Takakura, P. Meyrueis, Properties of a three-dimensional photonic jet, *Opt. Lett.* 30 (19) (2005) 2641–2643 <http://www.opticsinfobase.org/abstract.cfm?uri=OL-30-19-2641>.
- [107] A.V. Itagi, W.A. Challener, Optics of photonic nanojets, *JOSA A* 22 (12) (2005) 2847–2858 <http://www.opticsinfobase.org/abstract.cfm?uri=josaa-22-12-2847>.
- [108] A. Devilez, B. Stout, N. Bonod, E. Popov, Spectral analysis of three-dimensional photonic jets, *Opt. Express* 16 (18) (2008) 14200–14212, <https://doi.org/10.1364/OE.16.014200>.
- [109] Z. Chen, A. Taflove, X. Li, V. Backman, Superenhanced backscattering of light by nanoparticles, *Opt. Lett.* 31 (2) (2006) 196–198.
- [110] P. Ferrand, J. Wenger, A. Devilez, M. Pianta, B. Stout, N. Bonod, E. Popov, H. Rigneault, others, Direct imaging of photonic nanojets, *Opt. Express* 16 (10) (2008) 6930–6940 <http://www.opticsinfobase.org/abstract.cfm?uri=OE-16-10-6930>.
- [111] Z. Wang, W. Guo, L. Li, B. Luk'yanchuk, A. Khan, Z. Liu, Z. Chen, M. Hong, Optical virtual imaging at 50 nm lateral resolution with a white-light nanoscope, *Nat. Commun.* 2 (2011), 218, <https://doi.org/10.1038/ncomms1211>.
- [112] A. Heifetz, S.-C. Kong, A.V. Sahakian, A. Taflove, V. Backman, Photonic nanojets, *J. Comput. Theor. Nanosci.* 6 (9) (2009) 1979–1992, <https://doi.org/10.1166/jctn.2009.1254>.
- [113] A. Devilez, N. Bonod, J. Wenger, D. Gérard, B. Stout, H. Rigneault, E. Popov, Three-dimensional subwavelength confinement of light with dielectric microspheres, *Opt. Express* 17 (4) (2009) 2089–2094, <https://doi.org/10.1364/OE.17.002089>.
- [114] Y. Geints, E. Panina, A. Zemlyanov, Control over parameters of photonic nanojets of dielectric microspheres, *Opt. Commun.* 283 (23) (2010) 4775–4781, <https://doi.org/10.1016/j.optcom.2010.07.007>.
- [115] C.M. Ruiz, J.J. Simpson, Detection of embedded ultra-subwavelength-thin dielectric features using elongated photonic nanojets, *Opt. Express* 18 (16) (2010) 16805–16812 <https://www.osapublishing.org/abstract.cfm?uri=ol-18-16-16805>.
- [116] D.R. Mason, M.V. Jouravlev, K.S. Kim, Enhanced resolution beyond the Abbe diffraction limit with wavelength-scale solid immersion lenses, *Opt. Lett.* 35 (12) (2010) 2007–2009 <http://www.opticsinfobase.org/abstract.cfm?uri=ol-35-12-2007>.
- [117] J.Y. Lee, B.H. Hong, W.Y. Kim, S.K. Min, Y. Kim, M.V. Jouravlev, R. Bose, K.S. Kim, I.-C. Hwang, L.J. Kaufman, C.W. Wong, P. Kim, K.S. Kim, Near-field focusing and magnification through self-assembled nanoscale spherical lenses, *Nature* 460 (7254) (2009) 498–501, <https://doi.org/10.1038/nature08173>.
- [118] J.J. Schwartz, S. Stavrakis, S.R. Quake, Colloidal lenses allow high-temperature single-molecule imaging and improve fluorophore photostability, *Nat. Nanotechnol.* 5 (2) (2010) 127–132, <https://doi.org/10.1038/nnano.2009.452>.
- [119] T.R. Kumar, R.V. Krishnaiah, Optical Disk with Blu-Ray Technology, arXiv preprint arXiv, 2018 1310–1551 <http://arxiv.org/abs/1310.1551>.
- [120] M.-S. Kim, T. Scharf, S. Mühlig, C. Rockstuhl, H.P. Herzig, Engineering photonic nanojets, *Opt. Express* 19 (11) (2011) 10206–10220 <http://www.opticsinfobase.org/abstract.cfm?uri=oe-19-11-10206>.
- [121] M.-S. Kim, T. Scharf, M. Brun, S. Olivier, S. Nicoletti, H.P. Herzig, Advanced Optical Characterization of Micro Solid Immersion Lens, 2012 <https://doi.org/10.1117/12.921871> pp. 84300E–84300E–10.
- [122] M.-S. Kim, T. Scharf, D. Nguyen, E. Keeler, S. Rydberg, W. Nakagawa, G. Osowiecki, R. Voelkel, H.P. Herzig, J. Micro Nanolithography MEMS MOEMS 12 (2) (2013), 023015–023015, <http://spiedigitallibrary.org/article.aspx?articleid=1697307%20>.
- [123] D. Kang, C. Pang, S.M. Kim, H.S. Cho, H.S. Um, Y.W. Choi, K.Y. Suh, Shape-controllable microlens arrays via direct transfer of photocurable polymer droplets, *Adv. Mater.* 24 (13) (2012) 1709–1715, <https://doi.org/10.1002/adma.201104507>.
- [124] A. Darafsheh, G.F. Walsh, L. Dal Negro, V.N. Astratov, Optical super-resolution by high-index liquid-immersed microspheres, *Appl. Phys. Lett.* 101 (14) (2012), 141128, <https://doi.org/10.1063/1.4757600>.
- [125] A.V. Maslov, V.N. Astratov, Optical nanoscopy with contact Mie-particles: Resolution analysis, *Appl. Phys. Lett.* 110 (26) (2017), 261107, <https://doi.org/10.1063/1.4989687>.
- [126] D. Grojo, N. Sandeau, L. Boarino, C. Constantinescu, N. De Leo, M. Laus, K. Sparnacci, Bessel-like photonic nanojets from core-shell sub-wavelength spheres, *Opt. Lett.* 39 (13) (2014) 3989, <https://doi.org/10.1364/OL.39.003989>.

- [127] Y. Shen, L.V. Wang, J.-T. Shen, Ultralong photonic nanojet formed by a two-layer dielectric microsphere, *Opt. Lett.* 39 (14) (2014) 4120, <https://doi.org/10.1364/OL.39.004120>.
- [128] G. Gu, R. Zhou, Z. Chen, H. Xu, G. Cai, Z. Cai, M. Hong, Super-long photonic nanojet generated from liquid-filled hollow microcylinder, *Opt. Lett.* 40 (4) (2015) 625, <https://doi.org/10.1364/OL.40.000625>.
- [129] T. Jalali, D. Erni, Highly confined photonic nanojet from elliptical particles, *J. Mod. Opt.* 61 (13) (2014) 1069–1076, <https://doi.org/10.1080/09500340.2014.920056>.
- [130] R. Chen, J. Lin, P. Jin, M. Cada, Y. Ma, Photonic nanojets generated by rough surface micro-cylinders, *Electrical and Computer Engineering (CCECE)*, IEEE 28th Canadian Conference on, IEEE, 2015 2015, pp. 1393–1397, [http://ieeexplore.ieee.org/xpls/abs\\_all.jsp?arnumber=7129483](http://ieeexplore.ieee.org/xpls/abs_all.jsp?arnumber=7129483).
- [131] S. Lee, L. Li, Y. Ben-Aryeh, Z. Wang, W. Guo, Overcoming the diffraction limit induced by microsphere optical nanoscopy, *J. Opt.* 15 (12) (2013), 125710, <https://doi.org/10.1088/2040-8978/15/12/125710>.
- [132] A. Darafsheh, N.I. Limberopoulos, J.S. Derov, D.E. Walker, V.N. Astratov, Advantages of microsphere-assisted super-resolution imaging technique over solid immersion lens and confocal microscopies, *Appl. Phys. Lett.* 104 (6) (2014), 061117, <https://doi.org/10.1063/1.4864760>.
- [133] Y. Yan, L. Li, C. Feng, W. Guo, S. Lee, M. Hong, Microsphere-coupled scanning laser confocal nanoscope for sub-diffraction-limited imaging at 25 nm lateral resolution in the visible spectrum, *ACS Nano* 8 (2) (2014) 1809–1816, <https://doi.org/10.1021/nn406201q>.
- [134] H. Yang, N. Moullan, J. Auwerx, M.A.M. Gijs, Fluorescence imaging: super-resolution biological microscopy using virtual imaging by a microsphere nanoscope (Small 9/2014), *Small* 10 (9) (2014), <https://doi.org/10.1002/sml.201470055> 1876–1876.
- [135] A. Darafsheh, C. Guardiola, J. Finlay, A. Cárabe, D. Nihalani, Simple super-resolution biological imaging, *SPIE Newsroom* 2018, <https://doi.org/10.1117/2.1201503.005912>.
- [136] A. Darafsheh, C. Guardiola, D. Nihalani, D. Lee, J.C. Finlay, A. Cárabe, Biological Super-Resolution Imaging by Using Novel Microsphere-Embedded Coverslips, 2015 933705, <https://doi.org/10.1117/12.2078019>.
- [137] A. Darafsheh, C. Guardiola, A. Palovcak, J.C. Finlay, A. Cárabe, Optical super-resolution imaging by high-index microspheres embedded in elastomers, *Opt. Lett.* 40 (1) (2015) 5, <https://doi.org/10.1364/OL.40.000005>.
- [138] B. Du, Y.-H. Ye, J. Hou, M. Guo, T. Wang, Sub-wavelength image stitching with removable microsphere-embedded thin film, *Appl. Phys. A* 122 (1) (2018), <https://doi.org/10.1007/s00339-015-9528-y>.
- [139] H. Yang, M.A. Gijs, Optical microscopy using a glass microsphere for metrology of sub-wavelength nanostructures, *Microelectron. Eng.* 143 (2015) 86–90, <https://doi.org/10.1016/j.mee.2015.03.072>.
- [140] W. Fan, B. Yan, Z. Wang, L. Wu, Three-dimensional all-dielectric metamaterial solid immersion lens for subwavelength imaging at visible frequencies, *Sci. Adv.* 2 (8) (2016) e1600901–1600901, <https://doi.org/10.1126/sciadv.1600901>.
- [141] F. Wang, L. Liu, P. Yu, Z. Liu, H. Yu, Y. Wang, W.J. Li, Three-dimensional super-resolution morphology by near-field assisted white-light interferometry, *Sci. Rep.* 6 (2016), 24703, <https://doi.org/10.1038/srep24703>.
- [142] V.N. Astratov, A.V. Maslov, K.W. Allen, N. Farahi, Y. Li, A. Brettin, N.I. Limberopoulos, D.E. Walker, A.M. Urbas, V. Liberman, M. Rothschild, Fundamental Limits of Super-Resolution Microscopy by Dielectric Microspheres and Microfibers, 2016, 97210K, <https://doi.org/10.1117/12.2212762>.
- [143] D.N. Sitter, J.S. Goddard, R.K. Ferrell, Method for the measurement of the modulation transfer function of sampled imaging systems from bar-target patterns, *Appl. Opt.* 34 (4) (1995) 746–751.
- [144] R. Horstmeyer, R. Heintzmann, G. Popescu, L. Waller, C. Yang, Standardizing the resolution claims for coherent microscopy, *Nat. Photonics* 10 (2) (2016) 68–71.
- [145] L.A. Krivitsky, J.J. Wang, Z. Wang, B. Luk'yanchuk, Locomotion of microspheres for super-resolution imaging, *Sci. Rep.* 3 (1) (2018), <https://doi.org/10.1038/srep03501>.
- [146] Y. Li, Z. Shi, S. Shuai, L. Wang, Widefield scanning imaging with optical super-resolution, *J. Mod. Opt.* 62 (14) (2015) 1193–1197, <https://doi.org/10.1080/09500340.2015.1024774>.
- [147] P. Ghenuche, J. de Torres, P. Ferrand, J. Wenger, Multi-focus parallel detection of fluorescent molecules at picomolar concentration with photonic nanojets arrays, *Appl. Phys. Lett.* 105 (13) (2014), 131102, <https://doi.org/10.1063/1.4896852>.
- [148] J. Li, W. Liu, T. Li, I. Rozen, J. Zhao, B. Bahari, B. Kante, J. Wang, Swimming microrobot optical nanoscopy, *Nano Lett.* 16 (10) (2016) 6604–6609, <https://doi.org/10.1021/acs.nanolett.6b03303>.
- [149] F. Wang, L. Liu, H. Yu, Y. Wen, P. Yu, Z. Liu, Y. Wang, W.J. Li, Scanning superlens microscopy for non-invasive large field-of-view visible light nanoscale imaging, *Nat. Commun.* 7 (2016), 13748, <https://doi.org/10.1038/ncomms13748>.
- [150] M. Duocastella, F. Tantussi, A. Haddadpour, R.P. Zaccaria, A. Jacassi, G. Veronis, A. Diaspro, F.D. Angelis, Combination of scanning probe technology with photonic nanojets, *Sci. Rep.* 7 (1) (2018), <https://doi.org/10.1038/s41598-017-03726-5>.
- [151] G. Huszka, H. Yang, M.A.M. Gijs, Microsphere-based super-resolution scanning optical microscope, *Opt. Express* 25 (13) (2017), 15079, <https://doi.org/10.1364/OE.25.015079>.
- [152] B. Yan, Z. Wang, A.L. Parker, Y.-k. Lai, P. John Thomas, L. Yue, J.N. Monks, Superlensing microscope objective lens, *Appl. Opt.* 56 (11) (2017) 3142, <https://doi.org/10.1364/AO.56.003142>.
- [153] G. Huszka, M.A.M. Gijs, Turning a normal microscope into a super-resolution instrument using a scanning microlens array, *Sci. Rep.* 8 (1) (2018), <https://doi.org/10.1038/s41598-017-19039-6>.